remote sensing

MDPI

Article

Non-Dominated Sorting Genetic Algorithm II (NSGA2)-Based Parameter Optimization of the MSMGWB Model Used in Remote Infrared Sensing Prediction for Hot Combustion Gas Plume

Yihan Li, Haiyang Hu * and Qiang Wang

School of Energy and Power Engineering, Beihang University, Beijing 102206, China; yhli15@buaa.edu.cn (Y.L.)
* Correspondence: 09451@buaa.edu.cn

Abstract: The Multi-Scale Multi-Group Wide-Band (MSMGWB) model was used to calculate radiative transfer in strongly non-isothermal and inhomogeneous media such as the remote infrared sensing of aircraft exhaust system and jet plume scenario. In this work, the reference temperature was introduced into the model as an independent variable for each spectral subinterval group. Then, to deal with the exceedingly vast parameter sample space (i.e., the combination of spectral subinterval grouping results, reference temperatures and Gaussian quadrature schemes), an MSMGWB model's parameter optimization process superior to the exhaustive approach employed in previous studies was established, which was consisted of the Non-dominated Sorting Genetic Algorithm II method (NSGA2) and an iterative scan method. Through a series of 0-D test cases and two real 3-D remote infrared imaging results of an aircraft exhaust system, it was observed that the MSMGWB model established and optimiazed in current work demonstrated notable improvements in both accuracy and computational efficiency.

Keywords: remote infrared sensing; genetic algorithm; wide-band model; k-distribution

Citation: Li, Y.; Hu, H.; Wang, Q. Non-Dominated Sorting Genetic Algorithm II (NSGA2)-Based Parameter Optimization of the MSMGWB Model Used in Remote Infrared Sensing Prediction for Hot Combustion Gas Plume. *Remote Sens.* **2024**, *16*, 3116. https://doi.org/10.3390/rs16173116

Academic Editors: Hiren Jethva and Omar Torres

Received: 27 June 2024
Revised: 12 August 2024
Accepted: 20 August 2024
Published: 23 August 2024

1. Introduction

The remote infrared detection of aircraft is extensively applied in domains such as military and aerospace [1]. Among them, the solid walls and jets of the aircraft exhaust system, which have relatively high temperatures, are one of the main sources of infrared signals for detection [2]. The calculation and prediction of their remote infrared radiation possess significant engineering significance. The calculation of remote infrared radiation mainly encounters two issues: computational efficiency and accuracy [3]. Regarding the computational efficiency, as the gas radiation absorption spectrum differs from that of solids and is discontinuous, the calculation of the precise radiation transfer equation necessitates the adoption of a line-by-line (LBL) calculation approach [4]. However, this approach demands a considerable amount of computing capacity, severely restricting its application in engineering issues. Hence, several spectral band models have been developed and employed in recent years, such as k-distribution models [5–7], l-distribution models [8], statistical spectral band models [9–11], etc. From the aspect of accuracy, as the gas absorption coefficient oscillates intensely along the spectrum and changes unpredictably with the variation of thermodynamic states, these models are challenged by the radiation transfer calculation in strongly non-isothermal and inhomogeneous media.

For the given remote infrared radiation detection within the atmospheric radiation window band that does not require detailed spectral radiation characteristics, the wide-band model possesses the advantage in terms of computational effort in contrast to the narrow-band model [3]. The early wide-band models, such as the box model [12] and the exponential wide-band model [13,14], directly obtain the average parameters within

the spectral band. They are unable to capture and utilize the detailed spectral line information, frequently resulting in an average error of over 20% thus mainly concentrating on qualitative research. Yin employed the k-distribution model based on the principle of rearrangement of absorption coefficients to deal with the wide-band issue [15]. They made use of the spectral information to obtain the cumulative k-distribution function and decreased the average error to below 20%. The k-distribution model possesses two major advantages [16–18]: Firstly, it exhibits remarkable computational accuracy for radiation transfer in homogeneous gases and inhomogeneous gases that fulfill the correlated-k (CK) assumption, and the computational cost is merely a small portion of that of the LBL approach; Secondly, it is compatible with the methods of discretizing and solving the radiation transfer equation (RTE) in both differential and integral forms. However, the principal challenge in employing the aforementioned k-distribution model to solve the radiance issue such as the remote infrared imaging of the hot jet from an aircraft nozzle using hydrocarbon fuel is that the substantial disparity in the molar ratio and temperature of the radiative participating components between the combustion gas and the atmosphere can severely diminish the CK characteristics [19–21]. Studies have shown that the presence of "hot lines" in the absorption spectra of radiatively participating components exacerbates the disruption of CK characteristics due to temperature non-uniformity [22]. Current solutions to this issue can be categorized into the Multiple Line Group (MLG) [23–25] method and the Spectral Mapping Method (SMM) [26–28]. Both approaches involve dividing the concerned absorption spectra (SMM) or absorption lines (MLG) into several subsets to ensure that the absorption spectra of each subset maintain high CK characteristics across various thermodynamic states. The CK characteristic disruption caused by non-uniformity in component molar ratios is due to differences in the absorption spectra of the radiative participating components. Existing solutions include methods based on joint distribution functions [29], multiple integration [30] and various convolution [31]. Pal [32] incorporated both the convolution method [33] and the SMM method in the Full-Spectrum k-distribution (FSK) model, and the established Multi-Scale Multi-Group Full-Spectrum k-distribution (MSMGFSK) model can cope with the two CK characteristic failure mechanisms at the same time. Hu refined the same method to develop the MSMGWB model for wide-band applications, which was successfully applied to remote infrared sensing calculations [21]. However, any of the aforementioned methods for addressing the mechanisms that degrade CK characteristic come with increased computational demands, when using both the MS and MG methods to address two CK characteristic degradation issues. Therefore, both the MSMGFSK model and the MSMGWB model must be optimized to achieve the best balance between computational accuracy and cost.

Previous works have indicated that the random grouping initialization has a significant impact on the division results of the wavenumber subintervals, thus further affects the performance of the corresponding MSMGWB model [21]. Hu established an automatic optimization scheme to identify the optimal combination within the grouping results of the wavenumber subintervals and the Gaussian quadrature scheme [34]. Wang enhanced the scheme by augmenting the quantity of cases for the optimization objective function and the selection scope of Gaussian quadrature schemes, thereby obtaining model parameters with superior performance [35]. However, all the schemes of the aforementioned optimization platforms employ the exhaustive approach. As the optimization sample space increases, this approach has been incapable of obtaining optimization results within a time period measured in years.

The research contents of this study are as follows: In contrast to the previous work where the same reference temperature was employed among RTEs corresponding to each spectral subinterval group, the reference temperature within each group of the MSMGWB model was regarded as an independent variable for the first time, giving rise to three factors that require matching and optimization: the Gaussian quadrature points quantity, the reference temperature, and the spectral subinterval grouping results. The NSGA2 genetic algorithm was employed to obtain the optimal Gaussian quadrature points quantity

and reference temperature at given grouping results [36,37]. An iterative scan method was proposed to determine the most suitable grouping combination result, then the optimization results of three factors were obtained. Finally, the calculation results and costs of the MSMGWB model optimized in this work were compared with other models in a series of 0-D cases, as well as two 3-D cases where the parameters of the combustion gas and ambient air are completely different.

2. MSMGWB Model

The MSMGWB model was proposed to predict the remote infrared radiation emitted by hot combustion gas jets. The RTE without scattering gain can be written as

$$\begin{cases} \frac{dI_\eta}{ds} = (k_\eta(\phi) - k_{s\eta}(\phi))I_{b\eta} - k_\eta(\phi)I_\eta \\ I_{\Delta\eta} = \int_{\eta_L}^{\eta_U} I_\eta d\eta \end{cases} \tag{1}$$

where I_η is the spectral radiance, $I_{b\eta}$ the spectral radiance of blackbody, and s the location through the radiation transfer path. k_η and $k_{s\eta}$ are the spectral extinction and scattering coefficient at wavenumber η, respectively. In this work, $k_\eta = k_{s\eta} + \sum_{n=1}^{4} k_{n\eta}$, and $k_{s\eta} = k_{4s\eta}$, where n ranges from 1 to 4, corresponding to water vapor, carbon dioxide, carbon monoxide, and aerosol particles, respectively. $\phi = \phi(T, p, x, N)$ is the gas and particle thermodynamic state at a certain space location, including temperature, pressure, component concentration, and particle number density, which determines the local k_η and $k_{s\eta}$. η_L, η_U, and $\Delta\eta$ are the lower wavenumber, upper wavenumber, wavenumber range of current infrared bands user concerned, respectively. In this study, $k_{1\text{-}3\eta}$ is calculated by LBL based on HITEMP2010 database for gas components [38], while $k_{4\eta}$ and $k_{s\eta}$ by Mie scattering theory for aerosol [39,40].

In hot combustion gas remote detection scenario, water vapor and carbon dioxide are treated as participation in both emission and absorption process, while carbon monoxide and aerosols only contribute to the attenuation part, because they exist only in the atmosphere rather than in turbo gas. Besides, the emission and scattering gain from atmosphere are not considered here since they are commonly treated as background radiation and calculated separately. Therefore, Equation (1) can be simplified into [19,41]:

$$\begin{cases} \frac{dI_{n\eta}}{ds} = k_{n\eta} I_{b\eta}(T) - k_\eta I_{n\eta} \\ I_\eta = \sum_{n=1}^{2} I_{n\eta} \\ k_{3\eta} = k_{4\eta} = k_{4s\eta} = 0, \text{ in combustion gas} \\ I_{b\eta} = 0, \text{ in atmosphere} \end{cases} \tag{2}$$

where I_η is calculated by emission of water vapor and carbon dioxide while absorption and scattering of all four components.

Next, to establish and later enhance the relation between the cumulative distribution function of n-thcomponents $g_n(k_n, T_0)$ and the total extinction coefficient k of the mixed medium, the equation is given as

$$\begin{cases} \int_0^{g_n(k_n^*(g_n,T_0),T)} k_n(g_n, T) dg_n = \frac{1}{I_{b,\Delta\eta}(T)} \int_{\eta_L}^{\eta_U} k_{n\eta} H\left(k - k_\eta\right) I_{b\eta}(T) d\eta \\ g_n(k_n, T) = \frac{1}{I_{b,\Delta\eta}(T)} \int_{\eta_L}^{\eta_U} H\left(k_n - k_{n\eta}\right) I_{b\eta}(T) d\eta \end{cases} \tag{3}$$

where $I_{b,\Delta\eta}(T) = \int_{\eta_L}^{\eta_U} I_{b\eta}(T) d\eta$, k_n is the absorption coefficient of n-th components, H the Heaviside step function, and T_0 the reference temperature. Both k_η and k are monotonically increasing with $g_n(T_0)$ by Equation (3). Consequently, as derived in [34] Equation (2) is transformed based on the k-distribution theory to

$$\begin{aligned} &\frac{dI_{ng}}{ds} = k_n^*(g_n, T_0)a_n(k_n^*, T, T_0)I_{b,\Delta\eta}(T) - k(g_n, T_0)I_{ng} \\ &I_{\Delta\eta} = \sum_{n=1}^{2} I_n = \sum_{n=1}^{2} \int_0^1 I_{ng} dg_n(T_0) \end{aligned} \tag{4}$$

where k_n^* is a pseudo absorption coefficient of n-th components, and $a_n(k_n^*, T, T_0) = \frac{dg_n(k_n^*, T)}{dg_n(k_n^*, T_0)}$ is the non-gray stretch factor.

When the inhomogeneous medium contains only one participating component, it is obvious that Equation (4) is quivalent to Equation (1) if the extinction spectra is correlated, i.e., $g_n(\phi, k_{n\eta}, T_0) = F(k_{n\eta}(\phi_{ref}))|_{\forall\eta,\phi}^{n\equiv 1}$ where F is a monotonically increasing function, ϕ_{ref} is a reference thermodynamic state. Therefore, Equations (1) and (4) are equivalent only when equation

$$g_n(\phi, k_\eta, T_0) = F\Big(k_\eta(\phi_{ref})\Big)|_{\forall\eta,\phi} \tag{5}$$

holds for cases involving two or more participating components in inhomogeneous media [34,35]. Generally, $g_n(\phi, k_n, T_0)$ is not a constant for each η under various ϕ, introducing variations between the calculation results derived from Equations (1) and (4). This discrepancy is especially noticeable in scenarios with pronounced ϕ inhomogeneities.

The critical aspect of the MSMGWB model involves partitioning the wavenumber subintervals that constitute the absorption spectrum of the n-th component into M distinct subsets. The primary objective is to ensure that Equation (5) is satisfied within each subset of wavenumber subintervals to the greatest extent possible under the thermodynamic states of interest. Consequently, Equations (2)–(4) can be reformulated as

$$\begin{cases} \frac{dI_{nm\eta}}{ds} = k_{nm\eta}I_{b\eta}(T) - k_\eta I_{nm\eta} \\ I_\eta = \sum_{n=1}^{2}\sum_{m=1}^{M_n} I_{nm\eta} \\ k_{3\eta} = k_{4\eta} = k_{4s\eta} = 0, \text{ in combustion gas} \\ I_{b\eta} = 0, \text{ in atmosphere} \end{cases} \tag{6}$$

$$\begin{cases} \int_0^{g_{nm}\left(k_{nm}^*\left(g_{nm}, T_{nm}^0\right), T\right)} k_{nm}(g_{nm}, T)dg_{nm} = \frac{1}{I_{b,\Delta\eta}(T)} \int_{\eta_L}^{\eta_U} k_{nm\eta}H\left(k - k_\eta\right)I_{b\eta}(T)d\eta \\ g_{nm}(k_{nm}, T) = \frac{1}{I_{b,\Delta\eta}(T)} \int_{\eta_L}^{\eta_U} H\left(k_{nm} - k_{nm\eta}\right)I_{b\eta}(T)d\eta \end{cases} \tag{7}$$

$$\begin{cases} \frac{dI_{nmg}}{ds} = k_{nm}^*(g_{nm}, T_{nm}^0)a_{nm}(k_{nm}^*, T, T_{nm}^0) - k(g_{nm}, T_{nm}^0)I_{nmg} \\ I_{\Delta\eta} = \sum_{n=1}^{2}\sum_{m=1}^{M_n} I_{nm} = \sum_{n=1}^{2}\sum_{m=1}^{M_n} \int_0^1 I_{nmg} dg_{nm}(T_{nm}^0) \\ a_{nm}(k_{nm}^*, T, T_{nm}^0) = \frac{dg_{nm}(k_{nm}^*, T)}{dg_{nm}(k_{nm}^*, T_{nm}^0)} \end{cases} \tag{8}$$

It is different from the previous version MSMGWB model that an independent reference temperature was employed here, thus each group of each component has its own reference temperature T_{nm}^0 and Gaussian quadrature scheme. M_1 and M_2 are not constrained to be identical; they can take different values since the grouping of $k_{1\eta}$ and $k_{2\eta}$ is independent. The width of the wavenumber subintervals must be smaller than that in LBL, which was set at 0.005 cm^{-1} in this study. The grouping method is described as follows:

- **Step i.** Select the representative thermodynamic states encountered during the computation of atmospheric transmission characteristics for radiation emitted by hydrocarbon fuel combustion gases, as listed in Table 1.
- **Step ii.** Stochastically assign an initial group membership for each wavenumber subinterval within the absorption spectrum of the water vapor.
- **Step iii.** Compute M_1 group tags, which are given by

$$\xi_{nm\eta} = \sum_{i=1\sim 5}\sum_{i'=6\sim 9} ln^2\left(\frac{k_\eta(\phi_{i'})}{k(\phi_{i'}, g_{nm}(\phi_i, k_\eta, T_0), T_0)}\right) \tag{9}$$

for each wavenumber subinterval, followed by their redistribution to the group corresponding to the minimum $\xi_{nm\eta}$.

- **Step iv.** Iterate Step iii until fewer than 0.1% of the total $k_{1\eta}$ numbers change their group assignment.
- **Step v.** Repeat Steps ii~iv for each $k_{2\eta}$.

Table 1. Representative thermodynamic states for aeroengine jet plume and atmosphere.

Scenario	Thermodynamic State	$T(K)$	x_{H_2O}	x_{CO_2}	x_{CO}	$p(atm)$
Aeroengine jet plume	ϕ_1	1900	0.12	0.12	0	2
	ϕ_2	1900	0.12	0.12	0	1
	ϕ_3	1500	0.1	0.1	0	0.5
	ϕ_4	900	0.08	0.08	0	1
	ϕ_5	900	0.08	0.08	0	0.5
Atmosphere	ϕ_6	300	0.034	3.4×10^{-4}	1.42×10^{-7}	1
	ϕ_7	300	0.0068	3.4×10^{-4}	1.42×10^{-7}	1
	ϕ_8	293	0.02	3.4×10^{-4}	1.42×10^{-7}	0.9
	ϕ_9	263	0.002	3.4×10^{-4}	1.42×10^{-7}	0.5

It is obvious that $\xi_{nm\eta} = 0 | \forall \eta \in m\text{-}th \;\; group \;\; of \; n\text{-}th \; component$ means Equation (5) is true within m-th group of n-th component, i.e., $g_{nm}(\phi, k_\eta, T^0_{nm}) = F\Big(k_\eta(\phi_{ref})\Big)\Big|^{\forall\phi}_{\forall\eta_{nm}}$, where the η_{nm} is the wavenumber subinterval of the m-th group of the n-th component. In practice, the integration in the middle formula of Equation (8) is calculated by Gauss-Legendre quadrature, to give

$$\begin{cases} \frac{dI_{nm\bar{g},\bar{q}}}{ds} = \overline{\mathbf{A}}_{nm,\bar{q}}(T) I_{b,\Delta\eta}(T) - k(\overline{g}_{nm,\bar{q}}, T^0_{nm}) I_{nm\bar{g},\bar{q}} \\ I_{\Delta\eta} = \sum_{n=1}^{2} \sum_{m=1}^{M_n} I_{nm} = \sum_{n=1}^{2} \sum_{m=1}^{M_n} \sum_{\bar{q}=1}^{N_{nmg}} I_{nm\bar{g},\bar{q}} \\ I_{nm\bar{g},\bar{q}} = \int_{\tilde{g},m,\bar{q}-1}^{\tilde{g}_{nm,\bar{q}}} I_{nmg} dg_{nm}(T^0_{nm}) \\ \overline{A}_{nm,\bar{q}}(T) = \frac{1}{I_{b,\Delta\eta}(T)} \int_{\eta_U}^{\eta_L} k_{nm\eta} I_{b\eta}(T) H\big(k_{nm}(\tilde{g}_{nm,\bar{q}}, T^0_{nm}) - k_{nm\eta}\big) H\big(k_{nm\eta} - k_{nm}(\tilde{g}_{nm,\bar{q}-1}, T^0_{nm})\big) \\ 0 = \tilde{g}_{nm,0} < \overline{g}_{nm,1} < \tilde{g}_{nm,1} < \overline{g}_{nm,2} \cdots < \tilde{g}_{nm,\bar{q}-1} < \overline{g}_{nm,\bar{q}} < \tilde{g}_{nm,\bar{q}} < \\ \cdots < \tilde{g}_{nm,N_{nmg}-1} < \overline{g}_{nm,N_{nmg}} < \tilde{g}_{nm,N_{nmg}} = g_{nm}(\infty, T^0_{nm}) \end{cases} \tag{10}$$

where the N_{nmg} is the total number of $\overline{g}_{nm,\bar{q}}(T^0_{nm})$. Both $\frac{\overline{g}_{nm,\bar{q}}}{g_{nm}(\infty,T^0_{nm})}$ and $\frac{\tilde{g}_{nm,\bar{q}}}{g_{nm}(\infty,T^0_{nm})}$ are constants that solely denpend on the chosen Gauss quadrature schemes. It is worth noting that in contrast to the equation presented in [35] for the MSMGWB model, the sole disparity in the current study is that the reference temperature employed in each group is mutually independent.

The boundary solution of gray walls involving diffuse emitted and reflected radiation is transformed from Equation (8) as

$$\begin{aligned} I_{nm\bar{g},\bar{q},w} = & \frac{\varepsilon}{k\big(\phi_w, \bar{g}_{nm,\bar{q}}, T_w\big)} \overline{A}_{nm,\bar{q}}(\phi_w, T_w) I_{b,\Delta\eta}(T_w) \\ & + \frac{1-\varepsilon}{\pi} \int_0^{4\pi} I_{nm\bar{g},\bar{q}}(\vec{s}) \max(-\vec{n}_w \cdot \vec{s}, 0) d\Omega \end{aligned} \tag{11}$$

where $\phi_w = (T_w, p_w, x_w, N_w)$ represents the temperature and pressure at wall, gas component mole fractions and particle number densities of the medium adjacent to the wall, respectively. ε is the gray wall emissivity, $\vec{s}$ the (unit) direction vector of the incident radiation ($I_{nmg}(\vec{s})$), and Ω the solid angle corresponding to the $\vec{s}$, $\vec{n}_w$ the (unit) normal vector of the wall.

3. Parameter Optimization Method

The iteration process for group division of wavenumber subintervals, as mentioned earlier, resembles the standard k-means clustering algorithm. Like other methods of the k-means family, a distance needs to be defined as the basis for measuring the relationship between sample point and cluster center, and the distance in this work is defined by Equation (9). Consequently, akin to the standard k-means clustering, the final results of group division which directly determine the performance of MSMGWB model are significantly impacted by its initialization (Step ii in Section 2). Besides, the quadrature accuracy of Equation (8) may not exhibit a monotonic increase with increasing N_{nmg}, especially when the k-g_{nm} function contain stair-like zones, as depicted in Figure 1.

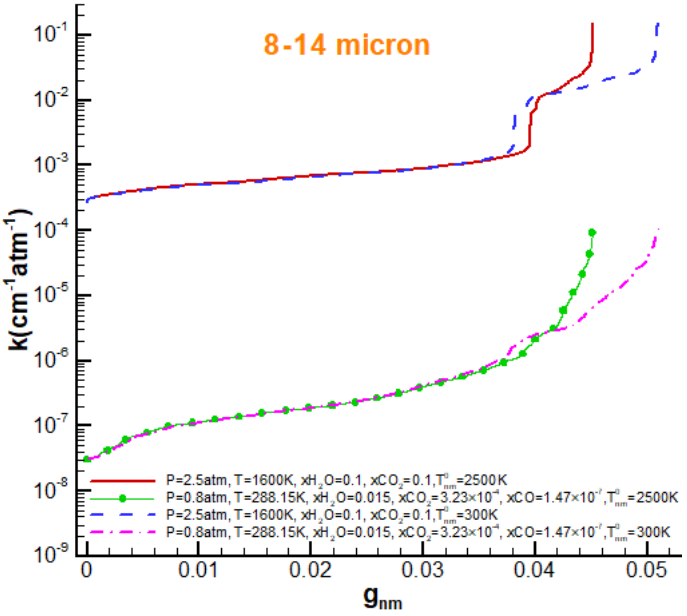

Figure 1. The relationship between k and g_{nm} of a group in different reference temperatures and thermodynamic states at 8~14 μm band.

Furthermore, the reference temperature value can also substantially impact correlated k-distribution models as reported in [34] and Figure 1. To identify the optimal combination of these three factors, we formulated an error function to gauge the performance of the MSMGWB model as

$$\begin{cases} f_{err} = \sum_{j=1}^{56} \begin{cases} error_{j,\max} & error_{j,\max} \le 0.08 \\ 0.08 + 10(error_{j,\max} - 0.08) & 0.08 < error_{j,\max} < 0.12 \\ 0.48 + 100(error_{j,\max} - 0.12) & error_{j,\max} \ge 0.12 \end{cases} \\ error_{j,\max} = \max\left(\left| \frac{I_{\Delta\eta,j,\mathrm{MSMGWB}}(L_a) - I_{\Delta\eta,j,\mathrm{LBL}}(L_a)}{I_{\Delta\eta,j,\mathrm{LBL}}(L_a)} \right| \right) \end{cases} \quad (12)$$

where j is the 56 0-D cases number (see in Appendix A), and it is obvious that the larger the $error_{j,max}$ is, the more punishment (represented as slope) of f_{err} gains. These 0-D cases is selected by typical scenarios of combustion gas and ambient atmosphere to comprehensively evaluate the performance of the MSMGWB model [34]. Figure 2 shows the effects of the wavenumber subinterval grouping results, the Gaussian quadrature points quantity, and the reference temperature on the f_{err}, respectively, when the other two factors are fixed at their optimal values. It is elucidated that all three factors significantly impact f_{err}. Besides, since we are pursuing the minimum value of f_{err}, the left part of the figure is more noteworthy. The red line shows lower probability density but big slope at small f_{err} area than the other two lines, i.e., the optimal Gaussian quadrature scheme is more difficult to be discovered than the other two factors.

In this section, the NSGA2 method will be employed to optimize the Gaussian quadrature points quantity and reference temperature for each group within an arbitrarily given water vapor and carbon dioxide grouping results combination. The optimization is based on the dual objective of quantitative accuracy and efficiency of the MSMGWB model. Concurrently, an iterative scheme driven by the NSGA2 optimization results will be established to select the optimal combination of water vapor and carbon dioxide grouping schemes.

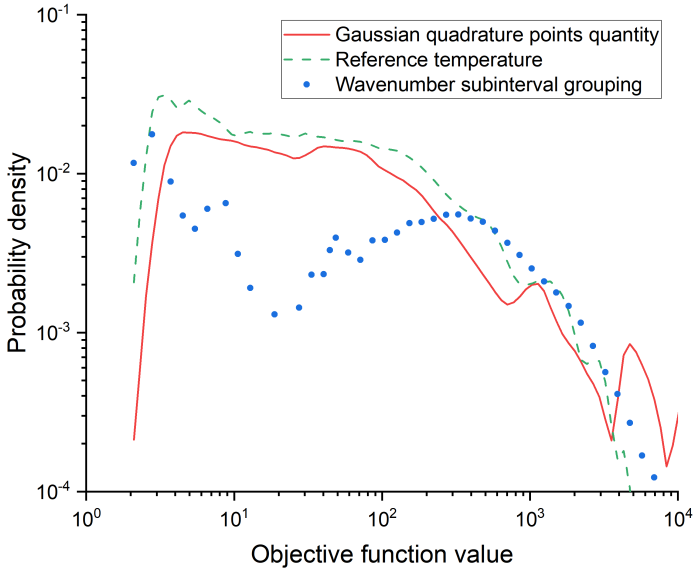

Figure 2. Relationship between probability density of objective function value and three critical factors (Gaussian quadrature point quantity, reference temperature, and wavenumber subinterval grouping).

3.1. Genotype Modeling

The genes chain consists of quadrature points quantity and reference temperature from each group. In 3~5 μm band, for instance, the spectra of H_2O and CO_2 are divided into 5 groups and 10 groups, respectively. Each group has its own Gaussian quadrature points quantity and reference temperature, therefore the length of the genes chain is 30. The quadrature points quantity range of each group is prescribed from 3 to 9 for feasible computational cost, and the reference temperature range is constrained from 100 K to 2500 K represented by 9 typical points. The variables in dark background color of the top chain in Figure 3 stand for quadrature points quantity of each group while the variables in light background color were the number of the corresponding reference temperature. Here we defined

$$f_N = \sum_{n=1}^{2} \sum_{m=1}^{M_n} N_{nmg} \tag{13}$$

which is directly proportional to the total Gaussian quadrature point quantity while solving RTE. Now, a certain gene chain is corresponding to certain parameters of the MSMGWB model, which also yields certain f_{err} and f_N.

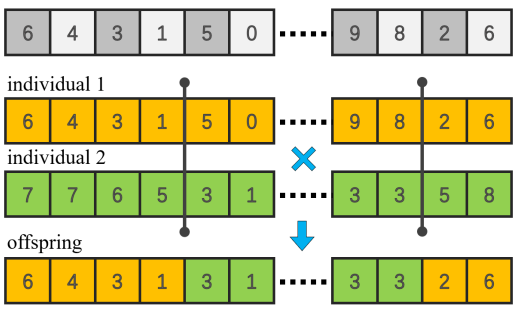

Figure 3. Genotype and crossover process diagram.

3.2. Non-Dominated Genetic Algorithm Process

The non-dominated genetic algorithm process is depicted in Figure 4 and basically consists of three steps as initializing, generating offspring, and ending iteration.

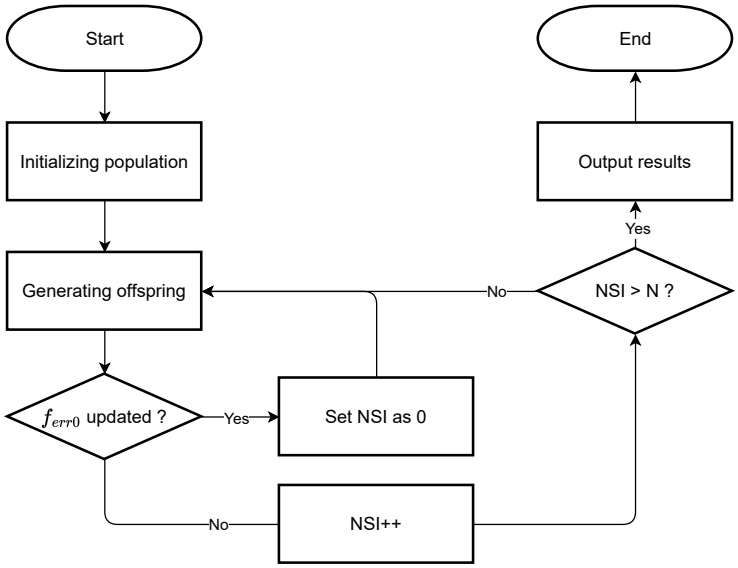

Figure 4. NSGA2 algorithm workflow diagram.

3.2.1. Initializing

Randomly generate an initial value for each gene in the genotype of every individual in the population.

3.2.2. Generating Offspring

As Figure 3 shows, generating offspring contains selection, crossover and mutation process. Firstly, conduct non-dominated sorting for all individuals in the parent population. An individual A is considered to dominate individual B only when both objective function values f_{err} and f_N of individual A are smaller than those of individual B. It is evident that each individual may dominate others and, in turn, be dominated by different individuals. The number of times an individual is dominated is referred to as its rank. A rank of 0 indicates that the individual is not dominated by any other individuals, and all individuals with a rank of 0 form the Pareto front of the current solution set.

Secondly, select parent individuals with the current rank of 0, duplicate them directly into the new offspring, and decrease the rank values of the individuals they dominate by 1. After this process a new generation of the current Pareto front is identified and duplicated into the new offspring. Repeat this operation until the number of parent individuals directly copied into the offspring reaches 50% of the entire population. Individuals within the same rank are first reordered then prioritized based on their crowding distance, given to

$$\begin{cases} d_i = \infty, i \in \{1, N_r\} \\ d_i = \frac{(f_{err,i+1} - f_{err,i-1})}{(f_{err,max} - f_{err,min})} + \frac{(f_{N,i+1} - f_{N,i-1})}{(f_{N,max} - f_{N,min})}, i \notin \{1, N_r\} \end{cases} \tag{14}$$

where 1 and N_r represent the first and the last individual after ascending reordering of f_{err} and f_N, respectively. A larger crowding distance implies higher genetic diversity in the solutions after the individual is added to the offspring, facilitating the expansion of the search space and reducing the risk of the iterative process getting trapped in local optima.

Finally, Another half of offspring are generated by crossover and mutation. Two parent individuals are randomly selected from the copied 50% advantageous population obtained in the second step, then they crossover by the probability P_c. During the crossover

process, two gene location points are randomly chosen, as depicted in Figure 3, to execute a two-point crossover and generate a new individual. In the absence of crossover by the probability P_c, one of the parent individuals is directly duplicated to create a new individual. Due to the stochastic crossover point selection, overlapping points can lead to single-point crossover. Moreover when both points are situated at the head or tail location of the genes chain, it reverts to no crossover, involving a direct duplication of the parent individual. After crossover, the individual randomly mutate by the number of mutation points and the probability P_m to finally generated a new individual into the offspring, as shown in Figure 5.

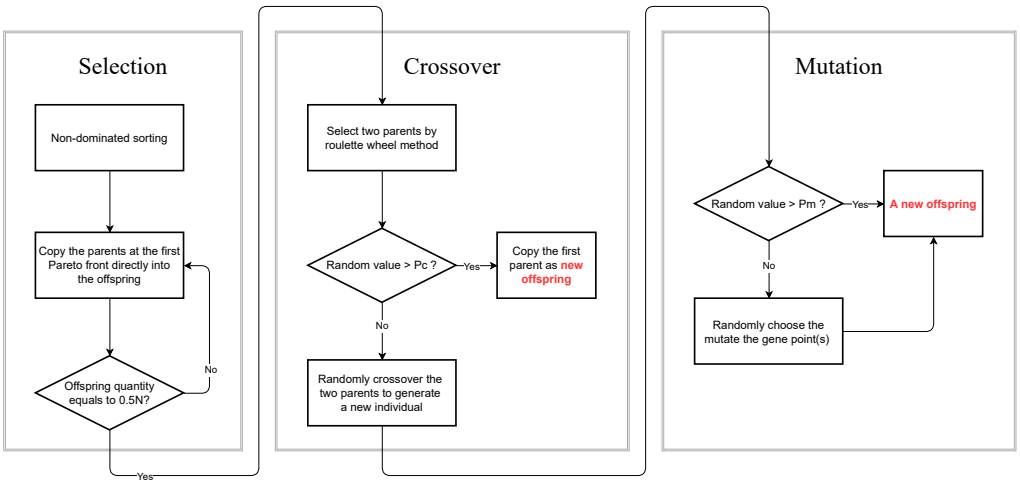

Figure 5. Offspring generation workflow diagram.

In this study, P_c is fixed at 0.8, while the P_m varies with the number of stagnant iterations of updating best solutions (NSI). When the NSI is less than 20, P_m is set to 0.05, and the number of mutation points is set to 1, while 0.2 and 2 as NSI no less than 20. Note that when the number of mutation points is set to 2, the mutation process will occur with an equal probability (50%–50%) between single-point mutation and two-points mutation. Upon each update of the best solutions, the NSI is reset to zero, which ensures the P_m stay at low value to avoid impeding convergence. When the NSI becomes high, it often indicates that the iteration process is nearing its conclusion or has reached a local optimum. In such scenarios, implementing a higher number of mutation points and an increased mutation probability aids in breaking out of local optima, thereby expanding the search space.

3.2.3. Iteration Ending

The iteration process is finished when the NSI reaches to 50 for it was proved by several repeated tests that 50 is large enough for the scale of this study to retain a convergence result.

3.2.4. Iteration Results

Figure 6a shows the fronts of a certain H_2O-CO_2 grouping results combination. It is observed that the spacing between fronts is exceedingly thin, corresponding to a convergent and dense result by genetic algorithm. Therefore, the smallest error function value of the first front, defined as f_{err0}, was served as the benchmark for assessing the iteration progress. Convergence process of f_{err0} for ten random grouping results combinations in 20,000 population size is depicted in Figure 6b. All of them began with a large f_{err0} for randomly initializing, descend rapidly, and eventually finish at a small stable f_{err0}.

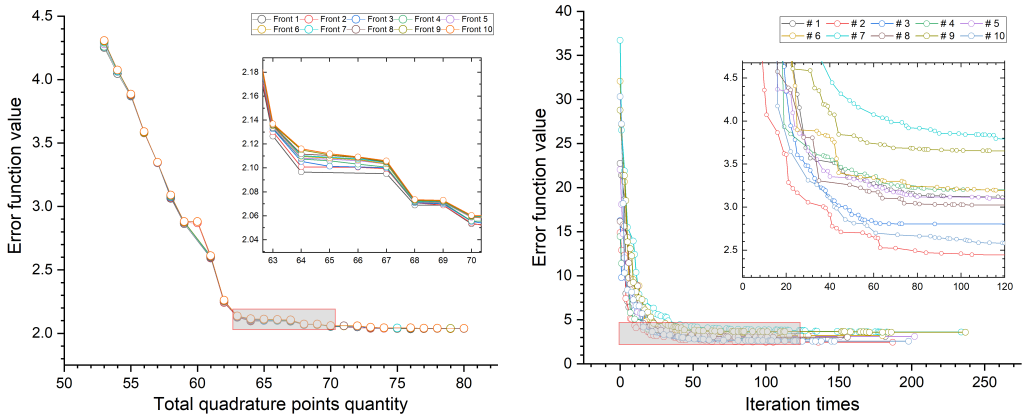

(**a**) (**b**)

Figure 6. Convergence results of the NSGA2 method: (**a**) the foremost 10 Pareto front results, (**b**) convergence iteration process of 10 random grouping strategy combinations.

To assess the accuracy of the genetic algorithm, we compared the results obtained by the genetic algorithm and exhaustive search in the 7.7~9.7 μm band which contains 11 H_2O groups and 2 CO_2 groups. Each group has 3 options for quadrature points quantity (3/5/7), and 2 options for reference temperatures (300 K/1900 K), resulting in a total of 13,060,694,016 possible combinations. As shown in Figure 7, the genetic algorithm produced results identical to those of the exhaustive search with a population size of 1000, while it costs five orders of magnitude less computational time than the exhaustive search.

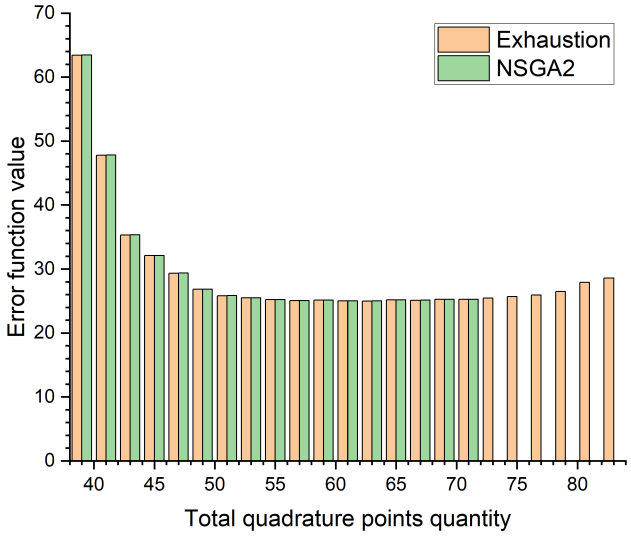

Figure 7. f_{err0} results between exhaustive search method and NSGA2 method.

3.3. Grouping Result Selection Based on an Iterative Scan Method

Due to the stochastic process in Step ii of wavenumber subintervals group division, it is nearly impossible to achieve good enough grouping results combinations between H_2O and CO_2 in few grouping experiments. Therefore, we produced about 10 to 10,000 grouping results for both H_2O and CO_2, then filter them for good combination by iteration method, as shown in Table 2 (S for the number of grouping results, subscript 1 and 2 for the H_2O and CO_2 respectively). Besides, for each group, the quadrature points quantity option is set to 7 (3 to 9), and the reference temperature is set to 7 (100 K to 2500 K). As a result, the combination quantity of quadrature points quantity, reference temperature, and grouping results is exceedingly large so that exhaustive search is totally incompetent. Two methods were proposed below to address the excessive computational complexity issue, reducing

the computational burden from quadratic growth with respect to the number of grouping results to linear growth, and finally collaborated with the non-dominated genetic algorithm to solve the optimization.

Table 2. Grouping result quantity and wavenumber group quantity of five typical infrared remote sensing bands for H_2O and CO_2.

Parameter	2~2.5 μm	3.7~4.8 μm	3~5 μm	7.7~9.7 μm	8~14 μm
S_1	3196	247	115	10,000	10,000
S_2	728	10,000	10,000	10	2172
M_1	15	5	5	11	10
M_2	5	10	10	2	10

3.3.1. Iterative Scan Method

To illustrate the problem in hand, 100 grouping results of H_2O and 400 grouping results for CO_2 were selected in 3~5 μm band, resulting in a total of 40,000 grouping combinations. Each combination's f_{err0} were computed using the genetic algorithm with a population size of 40,000 individuals per generation. The results, as shown in Figure 8, depict smaller f_{err0} in blue and larger f_{err0} in red.

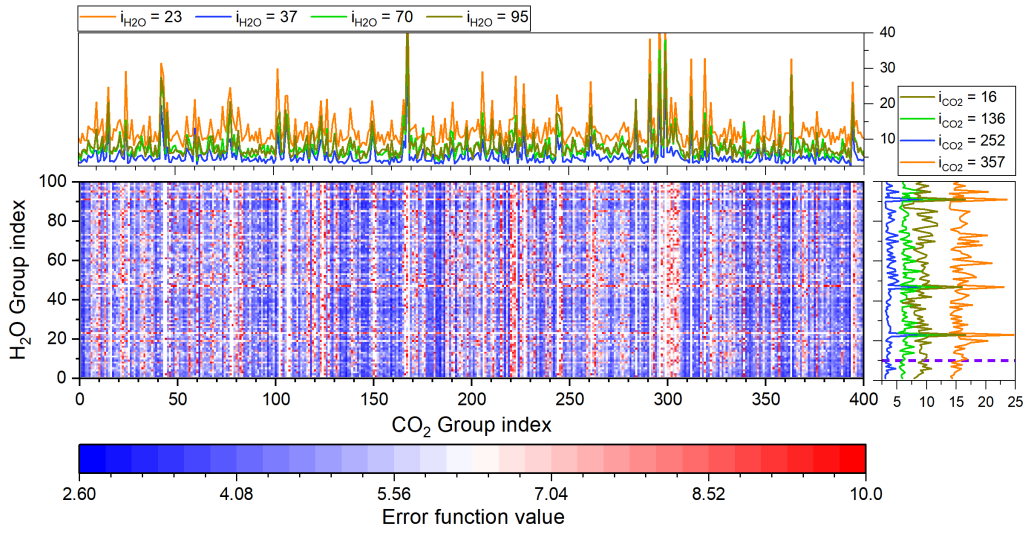

Figure 8. The f_{err0} results among 100 H_2O and 400 CO_2 grouping strategy combinations.

Four profile lines are randomly chosen for both H_2O and CO_2. These lines depict the f_{err0} of the local grouping result combination traversing all CO_2(H_2O) grouping results while keeping the H_2O(CO_2) grouping result fixed. In most cases, if CO_2 grouping result serial number (i_{CO_2}) at a certain position, for example $i_{CO_2} = 10$ as indicated by the purple dashed line in the figure, the inequality relation $f_{err0}^{i_{H_2O}} \leq f_{err0}^{i'_{H_2O}}$ holds, then for any value of i'_{CO_2}, $f_{err0}^{i_{H_2O}} \leq f_{err0}^{i'_{H_2O}}$ holds. The same is true for lines with $i_{H_2O} = \text{Const}$. Therefore, once the profile lines with low f_{err0} values for both H_2O and CO_2 are identified, the corresponding grouping results combinations are highly likely to contain the combination with the globally lowest f_{err0}. This probability increases as the number of selected low f_{err0} value profile lines grows. The scanning approach is as follows:

- **Step i.** Randomly select an i^1_{x,H_2O}, combine it with all i_{CO_2} and conduct the genetic algorithm iteration, arrange them in ascending order based on the f_{err0}, and identify the i^1_{1,CO_2} that results in the minimum f_{err0}.
- **Step ii.** Select the i^1_{1,CO_2} from step i, combine it with all i_{H_2O}, and conduct the genetic algorithm iteration, arrange them in ascending order based on the f_{err0}, and identify the i^2_{1,H_2O} that results in the minimum f_{err0}.
- **Step iii.** Select the i^2_{1,H_2O} from step ii, combine it with all i_{CO_2} and conduct the genetic algorithm iteration, and record the first p serial numbers with the smallest f_{err0} as a set $I_{CO_2} = \{i^3_{1,CO_2}, i^3_{2,CO_2}, \ldots, i^3_{p,CO_2}\}$.
- **Step iv.** Select the i^3_{1,CO_2} in I_{CO_2} from step iii, combine it with all i_{H_2O} and conduct the genetic algorithm iteration, and record the first q serial numbers with the smallest f_{err0} as a set $I_{H_2O} = \{i^4_{1,H_2O}, i^4_{2,H_2O}, \ldots, i^4_{q,H_2O}\}$.
- **Step v.** Combine the set I_{CO_2} and I_{H_2O}, then find out the optimal grouping result combination from the total $p \times q$ combinations.

where the superscript of i (e.g., i^2_{1,H_2O}) represents the step number in which the value is generated, and the first item of the subscript represents the order sorted by f_{err0}.

Considering the stochastic selection of i^1_{x,H_2O} in step i, the scanning approach introduces an additional iteration process to ensure the stability of the results. Clearly, with an increaseing number of iterations, both the results and stability improve, but the computational cost increases simultaneously. Therefore, we compared 4 different iteration approaches, evaluating the results when the total groups results for H_2O and CO_2 are taken in sets of 100 and 400, respectively. Each plan differs in the way I_{CO_2} and I_{H_2O} are obtained, while the remaining steps are the same. Plan A directly obtains I_{CO_2} and I_{H_2O} through steps i and ii only; Plan B follows the whole steps as described above; Plan C involves one more steps iii and iv than Plan B; Plan D repeats steps iii and iv multiple times, and filters out the grouping results corresponding to the higher 50% of f_{err0} at each step, until the remaining number of grouping results decreases to predefined numbers of p and q. As shown in Figure 9, blue cells represent scanned sample points, green cells represent the currently scanning sample point, and red cells represent the sample point with the lowest f_{err0} in the current scanning row (column), where the smaller f_{err0} the higher saturation of red color. Orange cells represent the finally selected sample points, i.e., the global optimal sample points obtained by the algorithm. Black cells represent excluded sample points by Plan D.

The performance of the 4 plans is demonstrated in Figure 10. The f_{err} results was obtained by averaging 100,000 repeated experiments for stability. The number of sample points is determined by the iterative scan method itself and the sizes of the sets I_{CO_2} and I_{H_2O}. Figure 9 illustrates the execution process of the four plans. It can be observed that Plan A, due to the randomness of Step i, cannot consistently obtain results with lower f_{err0}, and it descends slowly as the number of sample points increases. Plan C, involving multiple executions of steps iii and iv, leads to an increase in computational complexity, but quickly approaches the global optimum as the number of sample points increases. Plan D exhibits a good descending trend with the early increase in sample points, but the descent slows in the later stages, as some good grouping results are excluded prematurely. Plan B demonstrates results close to Plan C with a relatively small number of computation sample points. Therefore, it is adopted as a compromise between performance and efficiency.

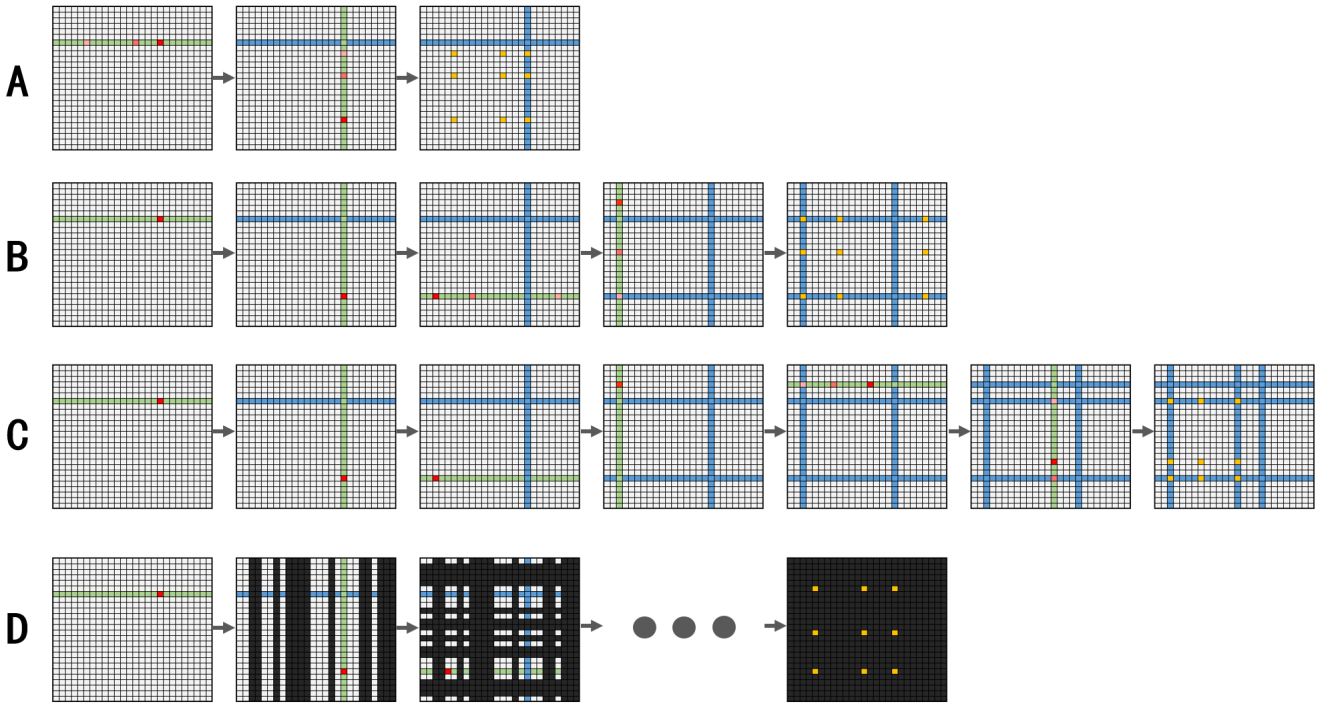

Figure 9. Diagram of 4 iterative scan method process plans.

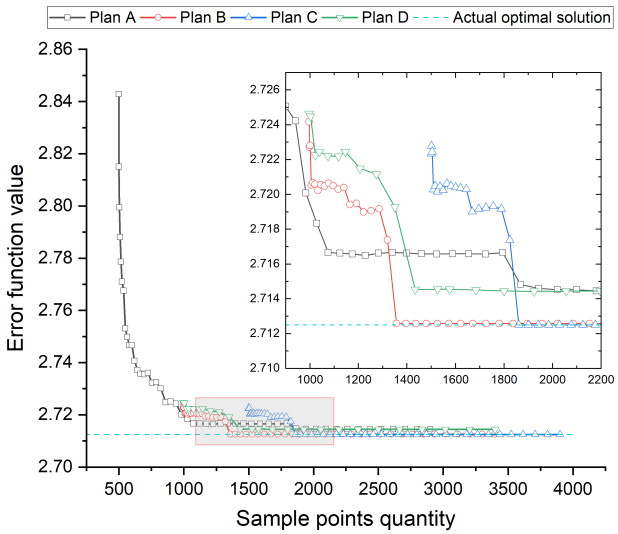

Figure 10. Convergence perfomance of 4 plans for scan iteration process.

3.3.2. Population Size Selection

Due to the enormous genotype sample space in this study, the genetic algorithm requires a large population size to achieve satisfactory results. However, the computational complexity of the NSGA2 increases quadratically with the population size. Therefore, the computational workload remains significant even with the iterative scanning approach adopted. As a result, some improvements need to be made at the population size level. In this section, 20 grouping results of both H_2O and CO_2 were randomly selected in 3~5 μm band, forming 400 grouping combination sample points. The genetic algorithm was then employed with 9 different population sizes (100, 200, 500, 1000, 2000, 5000, 10,000, 20,000, 40,000), and the f_{err0} obtained for each population was taken as the representative result.

As shown in Figure 11, the angular axis is divided into 400 parts representing 400 grouping results combinations, and the radial axis represents the population size. The results for

a population size of 40,000 is taken as the baseline, and the contour values represent the ratio between the f_{err0} of the model at current population size and the f_{err0} at the baseline population size. It can be observed that as the population size increases, the ratio gradually decreases towards 1, indicating an improvement in algorithm performance. When the population size reaches 20,000, the improvement is not significant. Additionally, Figure 12 analyzes the results for each grouping results combination at population size of 5000 and 40,000. The Spearman correlation analysis shows a high correlation coefficient of 0.920 and a low p-value of 0.000, indicating a strong correlation between them. It is also evident that for the same grouping results combination, the calculation result for a population size of 40,000 is significantly better than that for a population size of 5000 in the majority of grouping results combinations (corresponding to the points under the dash line), especially at those with smaller f_{err0}, which are exactly the grouping results combinations we are searching for. There are still few combination points above the dash line, however the most of them hold large f_{err0} and will not be selected in the iterative scan method. Since the steps i~iv of Plan B place a higher emphasis on the order of the results rather than their specific values, it is reasonable and accurate enough to utilize small population size in these steps. Note that there is approximate 8^2 times of workload between 5000 and 40,000 methods. Therefore, the completed approach is: steps i~iv employ a population size of 5000, while step v employs a population size of 40,000. This approach significantly improves computational efficiency without deteriorating the results.

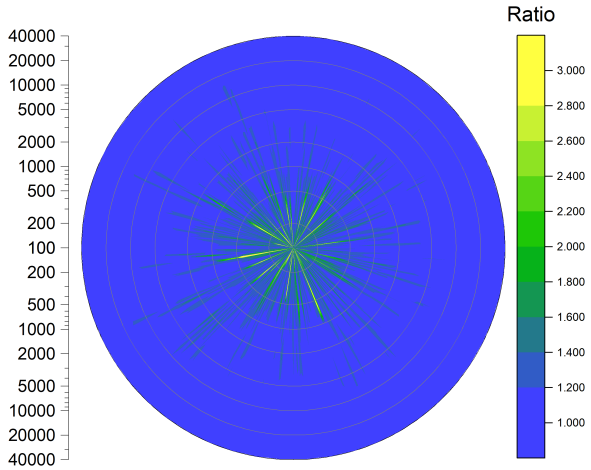

Figure 11. Ratio of the f_{err0} at the current sample population size to its corresponding baseline value.

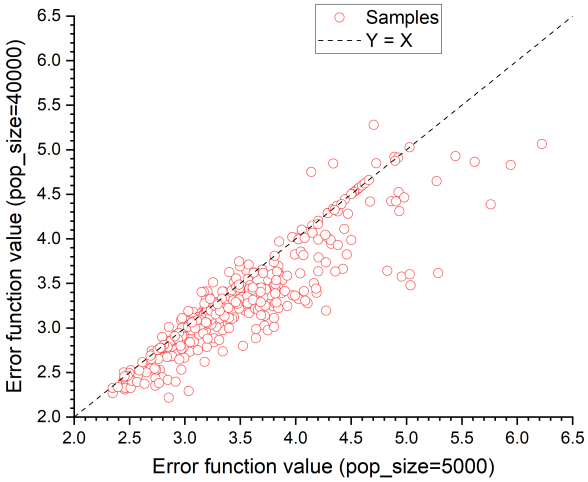

Figure 12. f_{err0} results between the same grouping result combination in the NSGA2 model population sizes of 5000 and 40,000.

4. Results

4.1. 0-D Cases

Adopting the methods established in last section, we optimized the MSMGWB model in grouping results combination, Gaussian quadrature points quantity, and reference temperature, at 5 typical atmospheric infrared window bands (2~2.5 μm, 3~5 μm, 7.7~9.7 μm, 8~14 μm), and Figures 13a–17a show the f_N versus f_{err} in each band. It is demonstrated that with increasing f_N, the f_{err} significantly reduces when f_N is at low level, while the reduction of f_{err} gradually becomes negligible at high f_N level and even showing an upward trend.

When compared to the current MSMGWB model [35], the MSMGWB model optimized in this work achieved significantly better computational accuracy in the vast majority of the test cases as shown in Figures 13b–17b and Table 3. The theoretical computational cost, i.e., the total number of solved RTE f_N of the 2~2.5 μm band, 3.7~4.8 μm band, 3~5 μm band, 7.7~9.7 μm band, and 8~14 μm band were decreased by 11.4%, 5.7%, 8.6%, 3.3%, and 11.6%, respectively. Meanwhile, the computational error (f_{err}) were decreased by 52.8%, 61.4%, 62.4%, 62.3%, 57.3% at the 5 bands, respectively. The finally selected points at the Pareto fronts are a trade-off consideration of f_N and f_{err}, as shown by the red points in the Figures 13a–17a.

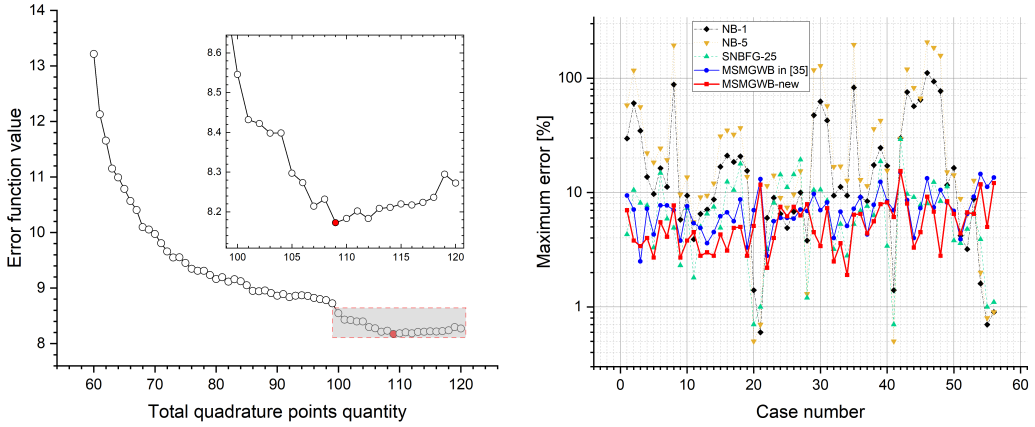

(**a**) (**b**)

Figure 13. Optimization results at 2~2.5 μm band: (**a**) Pareto front, (**b**) $error_{j,max}$ in 56 0-D cases.

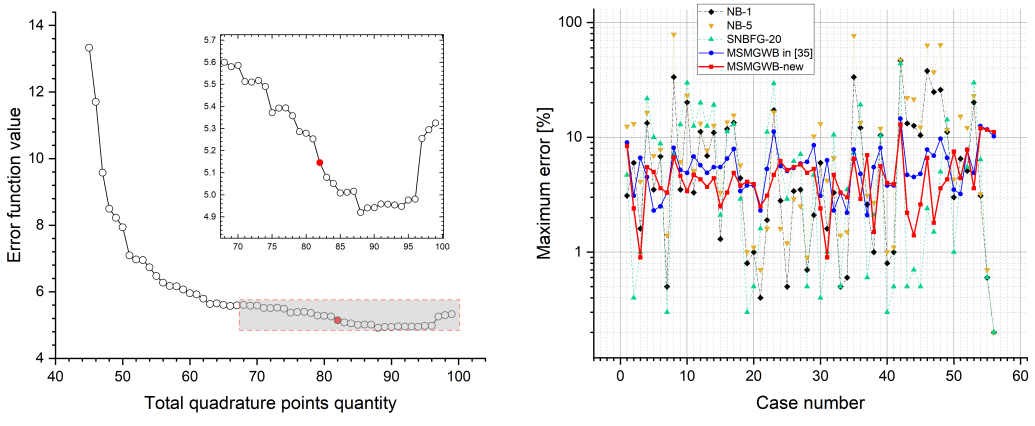

(**a**) (**b**)

Figure 14. Optimization results at 3.7~4.8 μm band: (**a**) Pareto front, (**b**) $error_{j,max}$ in 56 0-D cases.

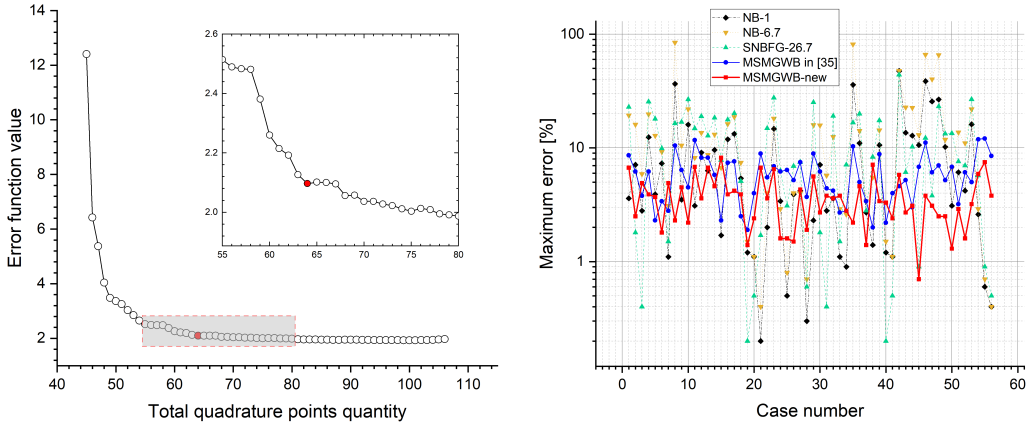

(**a**) (**b**)

Figure 15. Optimization results at 3~5 μm band: (**a**) Pareto front, (**b**) $error_{j,max}$ in 56 0-D cases.

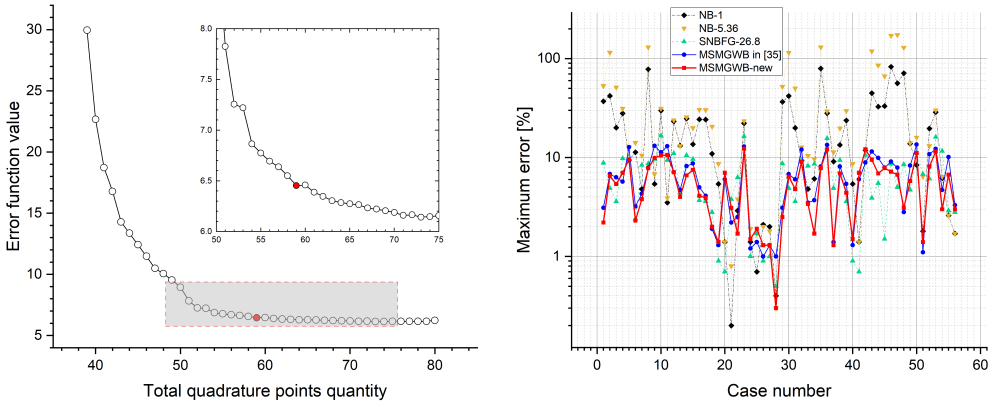

(**a**) (**b**)

Figure 16. Optimization results at 7.7~9.7 μm band: (**a**) Pareto front, (**b**) $error_{j,max}$ in 56 0-D cases.

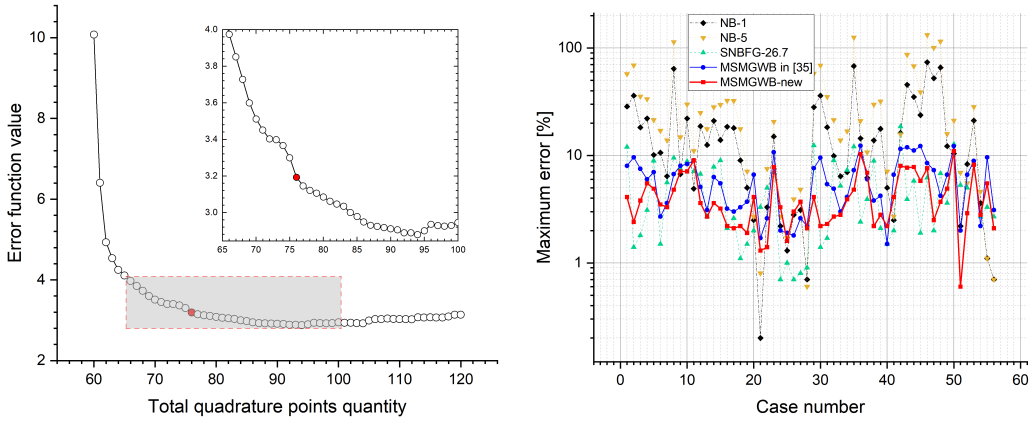

(**a**) (**b**)

Figure 17. Optimization results at 8~14 μm band: (**a**) Pareto front, (**b**) $error_{j,max}$ in 56 0-D cases.

Table 3. Comparison between the optimized MSMGWB model and other models.

	f_{err}				Number of Solved RTEs/Transmissivities			
Wave-band	MSMGWB-new	MSMGWB in [35]	SNBFG	NBKD	MSMGWB-new	MSMGWB in [35]	SNBFG	NBKD
2~2.5 μm	8.19	17.35	54.21	1212.4	109	123	272	3280
3.7~4.8 μm	5.15	13.33	130.9	51.0	82	87	216	10,300
3~5 μm	2.10	5.59	216.1	111.9	64	70	336	11,840
7.7~9.7 μm	6.30	16.72	24.23	1097.2	59	61	65	550
8~14 μm	3.4	7.01	12.86	1111.2	72	95	137	1730

4.2. Two High-Temperature Exhaust System 3-D Cases

Two 3-D cases of the high-temperature exhaust system cases were calculated. The MSMGWB model optimized in this work was used for remote infrared imaging and the error contours was obtained. These two 3-D cases have different exhaust system sizes, structures, working conditions, atmosphere parameters (see Tables 4 and 5), and aerosol spectral extinction characteristics (see Figure 18).

Table 4. Atmosphere thermodynamic state parameters at 0~7 km altitude in the large-sized case.

Altitude [km]	p [atm]	T [K]	x_{H_2O}	x_{CO_2}	x_{CO}
0~1	0.947	296.7	2.073×10^{-2}	3.301×10^{-4}	1.476×10^{-7}
1~2	0.843	290.7	1.925×10^{-2}	3.300×10^{-4}	1.426×10^{-7}
2~3	0.750	285.7	1.488×10^{-2}	3.298×10^{-4}	1.378×10^{-7}
3~4	0.665	280.4	6.619×10^{-3}	3.294×10^{-4}	1.331×10^{-7}
4~5	0.588	273.6	3.926×10^{-3}	3.296×10^{-4}	1.306×10^{-7}
5~6	0.519	267.0	2.761×10^{-3}	3.298×10^{-4}	1.295×10^{-7}
6~7	0.456	260.3	1.718×10^{-3}	3.302×10^{-4}	1.268×10^{-7}

Table 5. Atmosphere thermodynamic state parameters at 0~7 km altitude in the small-sized case.

Altitude [km]	p [atm]	T [K]	x_{H_2O}	x_{CO_2}	x_{CO}
0~1	0.938	258.1	1.350×10^{-3}	3.300×10^{-4}	1.481×10^{-7}
1~2	0.822	257.5	1.778×10^{-3}	3.298×10^{-4}	1.434×10^{-7}
2~3	0.719	254.3	1.629×10^{-3}	3.295×10^{-4}	1.377×10^{-7}
3~4	0.628	250.2	9.886×10^{-4}	3.295×10^{-4}	1.331×10^{-7}
4~5	0.547	244.3	6.202×10^{-4}	3.293×10^{-4}	1.307×10^{-7}
5~6	0.475	237.5	3.396×10^{-4}	3.295×10^{-4}	1.295×10^{-7}
6~7	0.411	230.7	1.946×10^{-4}	3.302×10^{-4}	1.268×10^{-7}

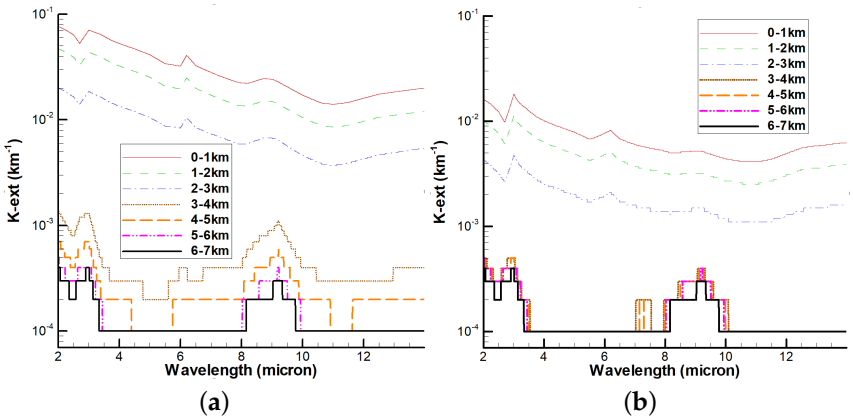

Figure 18. Aerosol spectral extinction coefficient at 0~7 km altitude and 2~14 μm: (**a**) large-sized case, (**b**) small-sized case.

For the large-sized case, as shown in Figure 19, the equivalent outlet diameter of the main nozzle of the supersonic exhaust system and the maximum diameter of the outer sleeve are 791 mm and 1220 mm, respectively. The inner wall of the main nozzle contains a heat shield and cooling structure, with a convergence angle of 35°. The working altitude of the nozzle is 7 km, the flight Mach number 0.7, the nozzle pressure ratio 2.38, the exhaust total temperature 900 K, and the surface emissivity of the material 0.8. The infrared detector is located on the ground and is 70 km away from the nozzle. The environmental atmosphere parameters are selected as the equatorial mode and the aerosol mode is selected as the 23-km visibility aerosol mode over the sea surface in the MODTRAN5 software. The infrared imaging resolution is 720 × 260 pixels, and the imaging direction forms an angle of 30° with the axis of the nozzle.

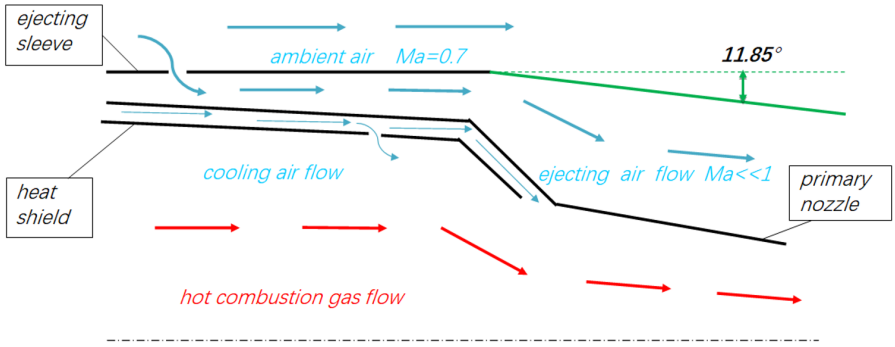

Figure 19. Diagram of the Large-sized exhaust system with a cooling structure.

The number of computational grids for the internal and external flow fields of this exhaust system is approximately 920,000. The calculation results show that there is a series of shock waves and expansion waves in internal fluid field and jet plume, as well as a complex-shaped combustion gas and environment air mixing layer, which causes the non-uniformity of the gas temperature, pressure, and mole fraction of components. However, although the mole fractions of water vapor and carbon dioxide change in the fluid field, their ratio is close to 1 everywhere (Figure 20). Due to the inclusion of the gas film cooling structure, solid wall temperature is relatively low (Figure 21).

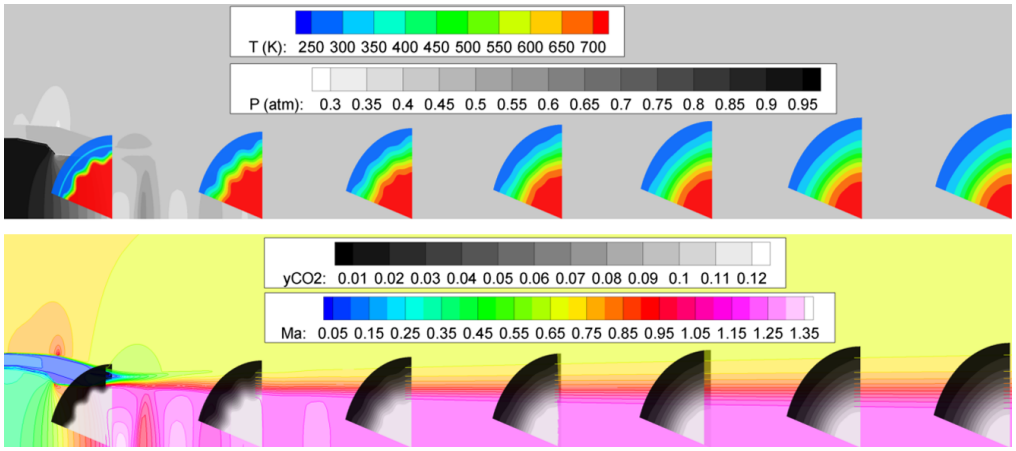

Figure 20. Distribution of temperature (T), pressure (p), carbon dioxide mass fraction (y_{CO_2}), and Mach number (Ma) in the meridional and axial sections of the fluid field of the large-sized exhaust system with a cooling structure.

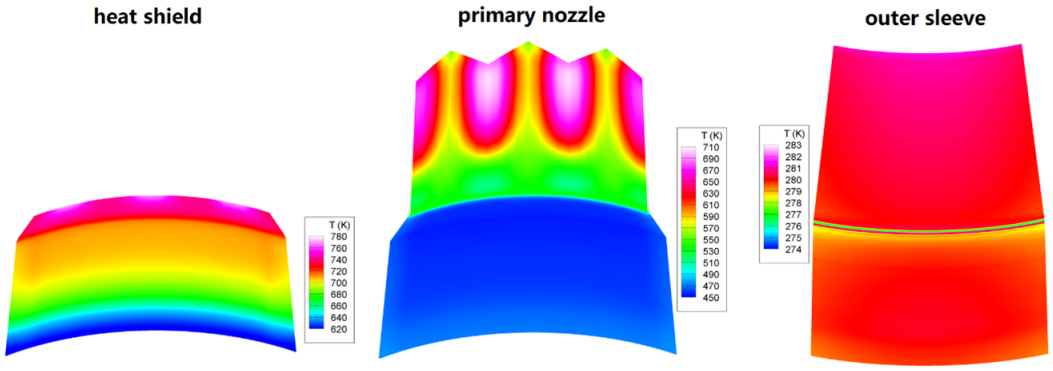

Figure 21. Temperature (T) distribution of the solid part of the large-sized exhaust system with a cooling structure.

The calculation results of long-distance infrared imaging at 2~2.5 μm, 3.7~4.8 μm, 3~5 μm, 7.7~9.7 μm, and 8~14 μm of this exhaust system and the calculation error distribution of the MSMGWB model are shown in Figure 22, with the latter based on the calculation results of the LBL model. Considering the computational cost of the LBL method, the radiative reflection of the solid wall is ignored.

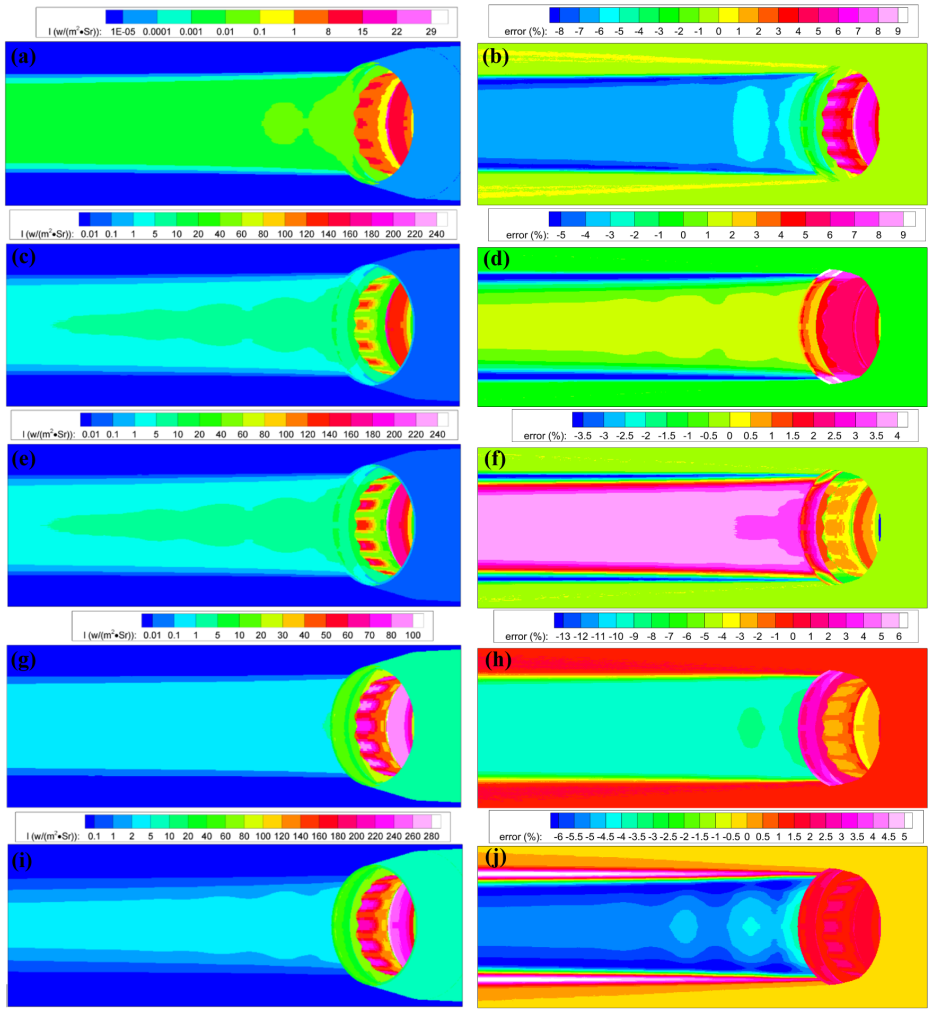

Figure 22. Remote infrared imaging of the large-sized exhaust system with a cooling structure in different atmospheric window bands (**left**), and the distribution of calculation errors of the optimized MSMGWB model (**right**), (**a**,**b**) 2~2.5 μm band, (**c**,**d**) 3.7~4.8 μm band, (**e**,**f**) 3~5 μm band, (**g**,**h**) 7.7~9.7 μm band, (**i**,**j**) 8~14 μm band.

4.3. Small-Sized High-Temperature Exhaust System 3-D Cases

For the small-sized case, as shown in Figure 23, the diameter of the throat and the maximum diameter of the outer sleeve are 128.6 mm and 152.4 mm, respectively. The high-temperature inner wall of the main nozzle has no cooling structure, with the convergence and divergence angles are 15.05° and 2.12° respectively. The working altitude of the nozzle is 0 km, the nozzle pressure ratio 10.1, the exhaust total temperature 1500 K, and the surface emissivity of the material 0.8. The infrared detector is located at an altitude of 7 km and is 50 km (for 2~2.5 μm band), 70 km (for 7.7~9.7 μm band), and 140 km (for other bands) away from the nozzle. The environmental atmosphere parameters are selected as the mid-latitudes winter mode and the aerosol mode is selected as the marine aerosol mode over the sea surface in the MODTRAN5.2.1.0 software.The infrared imaging resolution is 1000 × 400 pixels, and the imaging direction forms an angle of 30° with the axis of the nozzle.

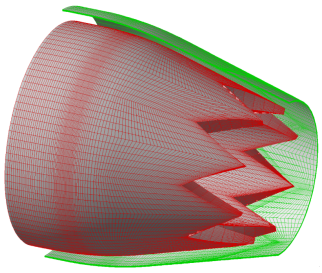

Figure 23. Diagram of the small-sized exhaust system without a cooling structure.

The number of computational grids for the internal and external flow fields of this exhaust system is approximately 890,000. The calculation results show that compared with the large-sized exhaust system, although the size is much smaller, the temperature and pressure of the exhaust jet are higher. Since it has the same V-shaped trailing edge as the large-sized exhaust system, the shape of the mixing layer between the jet plume and the ambient air is complex (Figure 24). Due to the higher exhaust temperature and the absence of a gas film cooling structure, the temperature of its solid structure is much higher than that of the large-sized case, and the temperature distribution of the main nozzle shows a distinct 3-D heat conduction effect. Moreover, the outer sleeve is affected by the radiative heat transfer from the outer wall of the main nozzle, and its temperature is significantly higher than the surrounding ambient temperature (Figure 25).

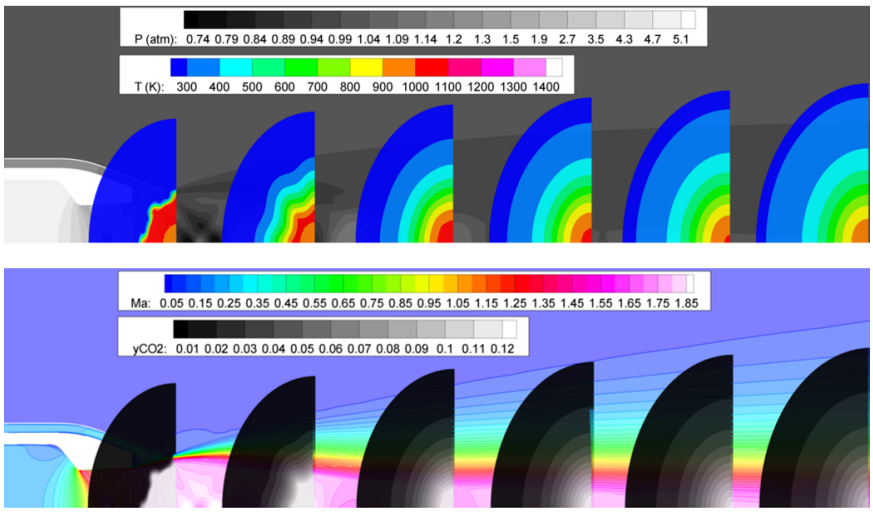

Figure 24. Distribution of temperature (T), pressure (p), carbon dioxide mass fraction (y_{CO_2}), and Mach number (Ma) in the meridional and axial sections of the fluid field of the small-sized exhaust system without a cooling structure.

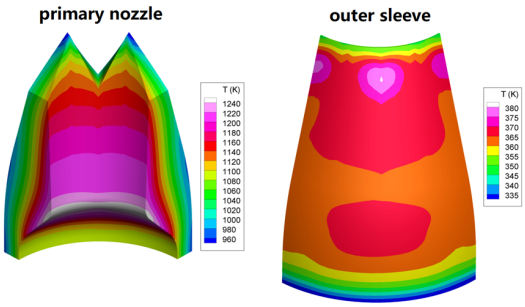

Figure 25. Temperature (T) distribution of the major components of the small-sized exhaust system without a cooling structure.

The same as in the large-sized case, Figure 26 shows the calculation results of long-distance infrared imaging and error distribution.

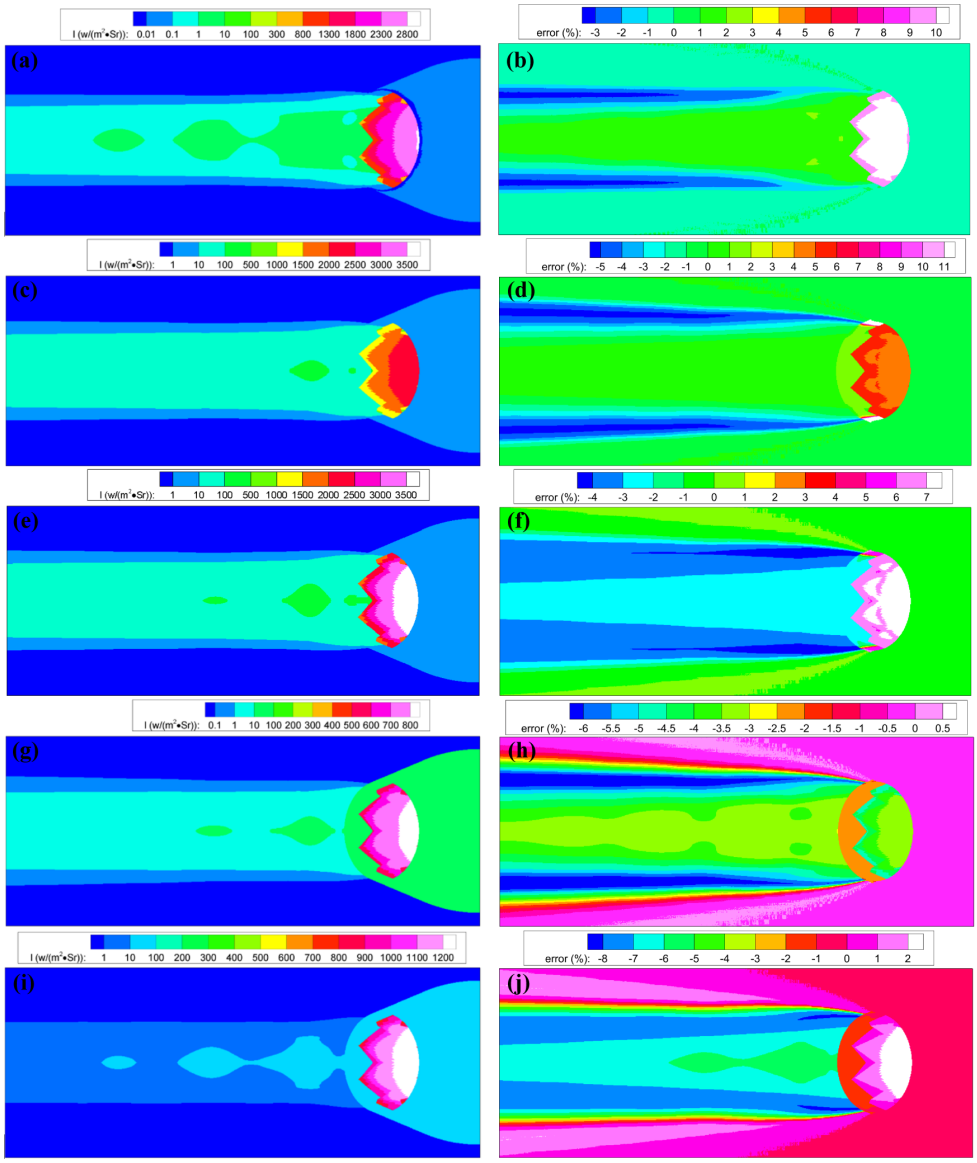

Figure 26. Remote infrared imaging of the small-sized exhaust system without a cooling structure in different atmospheric window bands (**left**) and the distribution of calculation errors of the optimized MSMGWB model (**right**), (**a**,**b**) 2~2.5 μm band, (**c**,**d**) 3.7~4.8 μm band, (**e**,**f**) 3~5 μm band, (**g**,**h**) 7.7~9.7 μm band, (**i**,**j**) 8~14 μm band.

As shown in Table 6, the max relative calculation error of both the large-sized case and small-sized case are no more than ±13% compared to the LBL results, which shows great accuracy with less computational cost than the previous MSMGWB model.

Table 6. Max relative error of the optimized MSMGWB model in two 3-D cases at five wave-bands.

Wave-Band	Max Relative Error (Large-Sized Case)	Max Relative Error (Small-Sized Case)
2~2.5 μm	−8.35/+9.95%	−3.24/+10.41%
3.7~4.8 μm	−6.19/+10.19%	−5.48/+12.17%
3~5 μm	−4.06/+3.78%	−4.43/+7.79%
7.7~9.7 μm	−9.84/+4.86%	−6.48/+0.04%
8~14 μm	−6.65/+5.56%	−8.49/+2.32%

5. Discussion

The Pareto front results of the NSGA2 algorithm show that as the number of RTE equations solved increases, the calculation accuracy is further improved, but there is a marginal diminishing effect (Figures 13a–17a). Note that we might not have deep enough search for the samples with big f_N and overrate the f_{err0} of them, because the central limit theorem leads few individuals with big f_N at the initialization step of NSGA2, meanwhile a part of the driving force for the NSGA2 iterations is directed towards generating individuals with smaller f_N. However, due to the compromise considerations of f_N and f_{err0}, the samples with big f_N were not considered in practice for their disadvantage in computational efficiency.

Even though this study made progress in the modeling and parameter optimization of the MSMGWB model, several issues warrant further exploration. Firstly, In addition to the four main substances adopted in this work, there are some other radiative absorption components in the atmosphere (such as methane, nitrous oxide, etc.). More accurate calculations need to take all these components into account. Secondly, the number of groups for water vapor and carbon dioxide will also affect the calculation accuracy and efficiency of the model. After adding the remaining atmospheric components in the second point, this parameter needs to be updated. In the future work, we will commence from the aforementioned contents and keep enhancing the performance and universality of the MSMGWB model.

6. Conclusions

In this study, compared with the MSMGWB models where each spectral subinterval group shares the same reference temperature [34,35,42], we proposed to optimize the reference temperature as an independent parameter within each group. To deal with the increase in the number of model parameter combinations, the NSGA2 genetic algorithm and an iterative scan method were introduced, and it was demonstrated that the above algorithms can obtain the optimal model parameters combination. The calculation results of 0-D and 3-D cases show that the MSMGWB model optimized based on the above algorithms has significantly improved computational efficiency and accuracy in 5 atmospheric infrared window wavebands compared to the present MSMGWB model.

Other conclusions were drawn as follows:

The Gaussian quadrature scheme has a greater influence on the computational accuracy of the MSMGWB model than the spectrum grouping results and reference temperature; A population size of 20,000 is sufficient for parameter optimization of the MSMGWB model based on the NSGA2 algorithm; At the scanning and screening stage of spectrum grouping results combinations, 5000 of population is enough and can greatly reduce the calculation time; The spectrum grouping result of water vapor and carbon dioxide has an approximately independent influence on the accuracy of the MSMGWB model. Therefore, the iterative scan method can be used to quickly obtain the optimal grouping results combination.

Author Contributions: Conceptualization, H.H. and Y.L.; methodology, Y.L.; software, Y.L.; validation, Y.L., H.H. and Q.W.; formal analysis, Y.L.; investigation, Y.L.; resources, Y.L.; data curation, Y.L.; writing—original draft preparation, Y.L.; writing—review and editing, Y.L., H.H. and Q.W.; visualization, Y.L.; supervision, Y.L.; project administration, H.H.; funding acquisition, H.H. All authors have read and agreed to the published version of the manuscript.

Funding: This research was funded by J2019-III-0009-0053 National Science and Technology Major Project, and the APC was funded by National Science and Technology Major Project.

Data Availability Statement: The source code of this work can be found at this website, https://github.com/1oyue/mdpi_data, accessed on 19 August 2024.

Acknowledgments: We thank the School of Energy and Power Engineering, Beihang University for its help in this project.

Conflicts of Interest: The authors declare no conflicts of interest. The funders had no role in the design of the study; in the collection, analyses, or interpretation of data; in the writing of the manuscript; or in the decision to publish the results.

Appendix A

As shown in Figure A1, there are two types of radiative transfer paths in this study among 56 0-D cases. In the first type, radiance emits through a hot combustion gas with a transmission path length L_h (which holds constant in the 0-D case calculation), then attenuates though the atmosphere under various transmission distances L_c. In the second type, radiance emits from a black wall and is attenuated by the atmosphere after passing through a hot gas layer and a cold gas layer with constant path lengths of L_h and L_c, respectively. The detailed parameters of the cases are shown in Table A1.

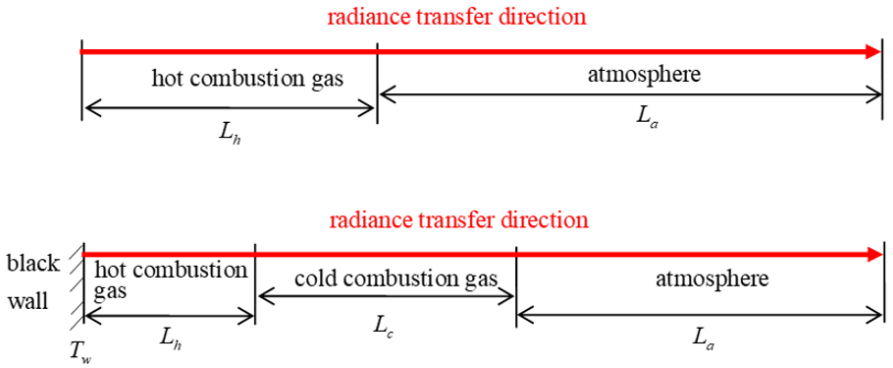

Figure A1. Two types of radiative transfer paths, diagram of 56 0-D cases.

Table A1. Thermal dynamic states table of 56 0-D cases.

	Hot Gas Parameters						Cold Gas Parameters						Environmental Atmospheric Parameters					
Number	L_h **[cm]**	p **[atm]**	T **[K]**	x_{H_2O}	x_{CO_2}	T_w **[K]**	L_c **[cm]**	p **[atm]**	T **[K]**	x_{H_2O}	x_{CO_2}	x_{CO}	L_a **[cm]**	p **[atm]**	T **[K]**	x_{H_2O}	x_{CO_2}	x_{CO}
1	50	1	800	0.1	0.1								40	1	308.15	0.05724	3.23×10^{-4}	1.47×10^{-7}
2	50	1	600	0.1	0.1								40	1	288.15	0.00184	3.23×10^{-4}	1.47×10^{-7}
3	50	1	800	0.1	0.1								40	1	288.15	0.00184	3.23×10^{-4}	1.47×10^{-7}
4	80	1.5	1300	0.1	0.1								100	0.9	298.15	0.03226	3.23×10^{-4}	1.47×10^{-7}
5	80	1	1300	0.1	0.1								100	1	298.15	0.03226	3.23×10^{-4}	1.47×10^{-7}
6	80	2	1300	0.1	0.1								100	0.8	285.2	0.00959	3.23×10^{-4}	1.39×10^{-7}
7	80	1	1300	0.1	0.1								100	1	298.15	0.03226	3.23×10^{-4}	1.47×10^{-7}
8	80	1	400	0.11	0.11								40	1	300	0.0323	3.23×10^{-4}	1.47×10^{-7}
9	80	1	1600	0.11	0.11								100	1	300	0.0323	3.23×10^{-4}	1.47×10^{-7}
10	80	2	1600	0.11	0.11								100	0.9	300	0.0323	3.23×10^{-4}	1.47×10^{-7}
11	80	1	1900	0.12	0.12								100	1	300	0.0323	3.23×10^{-4}	1.47×10^{-7}
12	80	1.5	1900	0.12	0.12								100	0.9	300	0.0323	3.23×10^{-4}	1.47×10^{-7}
13	80	1.5	1900	0.12	0.12								100	0.9	294.2	0.0184	3.23×10^{-4}	1.47×10^{-7}
14	70	1.6	1800	0.14	0.12								100	0.8	300	0.03	3.23×10^{-4}	1.47×10^{-7}
15	60	1	1050	0.1	0.1								80	1	294.2	0.0184	3.23×10^{-4}	1.47×10^{-7}
16	60	2	1050	0.1	0.1								80	0.9	294.2	0.0184	3.23×10^{-4}	1.47×10^{-7}
17	60	2	1050	0.1	0.1								80	1	294.2	0.0184	3.23×10^{-4}	1.47×10^{-7}
18	60	2	1050	0.1	0.1								80	0.7	279.2	0.00595	3.28×10^{-4}	1.34×10^{-7}
19	100	0.42	1500	0.08	0.08								200	0.42	254.7	0.00102	3.30×10^{-4}	1.25×10^{-7}
20	100	0.177	1800	0.1	0.1								200	0.177	215.8	8.01×10^{-6}	3.30×10^{-4}	6.38×10^{-8}
21	50	1	1500	0.1	0.1	900	150	1	550	0.05	0.05		100	0.9	300	0.0323	3.23×10^{-4}	1.47×10^{-7}
22	50	1	1500	0.1	0.1	450	150	1	550	0.05	0.05		100	0.9	300	0.0323	3.23×10^{-4}	1.47×10^{-7}
23	50	2	1500	0.1	0.1	450	150	1	550	0.05	0.05		100	0.9	300	0.0323	3.23×10^{-4}	1.47×10^{-7}
24	50	2.5	1700	0.1	0.1	650	300	1	550	0.05	0.05		200	0.62	273.2	0.0038	3.29×10^{-4}	1.31×10^{-7}
25	50	1.5	1700	0.1	0.1	650	300	1	550	0.05	0.05		200	0.62	273.2	0.0038	3.29×10^{-4}	1.31×10^{-7}
26	50	2.5	1700	0.1	0.1	650	100	1	550	0.05	0.05		200	0.62	273.2	0.0038	3.29×10^{-4}	1.31×10^{-7}
27	50	2.5	1400	0.1	0.1	450	300	1	550	0.05	0.05		200	0.62	273.2	0.0038	3.29×10^{-4}	1.31×10^{-7}
28	50	0.7	1800	0.12	0.12	500	150	0.48	550	0.1	0.1		200	0.32	241.7	4.13×10^{-4}	3.30×10^{-4}	1.09×10^{-7}
29	50	1	800	0.1	0.1								40	1	308.15	0.05724	3.23×10^{-4}	1.47×10^{-7}
30	50	1	600	0.1	0.1								40	1	288.15	0.00184	3.23×10^{-4}	1.47×10^{-7}

Table A1. *Cont.*

	Hot Gas Parameters						Cold Gas Parameters						Environmental Atmospheric Parameters					
Number	L_h **[cm]**	p **[atm]**	T **[K]**	x_{H_2O}	x_{CO_2}	T_w **[K]**	L_c **[cm]**	p **[atm]**	T **[K]**	x_{H_2O}	x_{CO_2}	x_{CO}	L_a **[cm]**	p **[atm]**	T **[K]**	x_{H_2O}	x_{CO_2}	x_{CO}
31	50	1	800	0.1	0.1								40	1	288.15	0.00184	3.23×10^{-4}	1.47×10^{-7}
32	80	1	1300	0.1	0.1								100	1	298.15	0.03226	3.23×10^{-4}	1.47×10^{-7}
33	80	1	1300	0.1	0.1								100	1	298.15	0.03226	3.23×10^{-4}	1.47×10^{-7}
34	80	1	1300	0.1	0.1								30	1	298.15	0.03226	3.23×10^{-4}	1.47×10^{-7}
35	80	1	400	0.11	0.11								40	1	300	0.0323	3.23×10^{-4}	1.47×10^{-7}
36	80	2	1600	0.11	0.14								60	0.9	300	0.0323	3.23×10^{-4}	1.47×10^{-7}
37	2	1.6	1800	0.14	0.12								20	0.8	300	0.024	3.23×10^{-4}	1.47×10^{-7}
38	60	1	1050	0.1	0.1								80	1	294.2	0.0184	3.23×10^{-4}	1.47×10^{-7}
39	60	2	1050	0.1	0.1								80	0.9	294.2	0.0184	3.23×10^{-4}	1.47×10^{-7}
40	100	0.42	1500	0.08	0.08								200	0.42	254.7	0.00102	3.30×10^{-4}	1.25×10^{-7}
41	100	0.177	1800	0.1	0.1								200	0.177	215.8	8.01×10^{-6}	3.30×10^{-4}	6.38×10^{-8}
42	50	1	1500	0.1	0.1		150	1	550	0.05	0.05		100	0.9	300	0.0323	3.23×10^{-4}	1.47×10^{-7}
43	15	0.8	650	0.1	0.1								100	0.8	288.15	0.005	3.23×10^{-4}	1.47×10^{-7}
44	5	1	750	0.1	0.1								100	0.8	288.15	0.01	3.23×10^{-4}	1.47×10^{-7}
45	5	0.5	900	0.1	0.1								120	0.5	263.15	0.002	3.23×10^{-4}	1.47×10^{-7}
46	10	0.5	500	0.1	0.1								40	1	293.15	0.015	3.23×10^{-4}	1.47×10^{-7}
47	10	1	550	0.12	0.1								100	0.6	273.15	0.004	3.23×10^{-4}	1.47×10^{-7}
48	10	1	500	0.1	0.12								80	1	300	0.012	3.23×10^{-4}	1.47×10^{-7}
49	150	2.5	1600	0.1	0.1								100	0.8	288.15	0.015	3.23×10^{-4}	1.47×10^{-7}
50	10	0.5	1500	0.13	0.1								120	0.9	293.15	0.02	3.23×10^{-4}	1.47×10^{-7}
51	70	1	1400	0.12	0.12	400	30	1	300	0.03	3.4×10^{-4}	1.47×10^{-7}	120	0.6	260	0.0015	3.30×10^{-4}	1.31×10^{-7}
52	150	0.6	1700	0.1	0.12	600	10	0.6	260	0.0015	3.3×10^{-4}	1.31×10^{-7}	40	1	300	0.03	3.30×10^{-4}	1.47×10^{-7}
53	80	2	1600	0.11	0.14								100	0.9	300	0.0323	3.23×10^{-4}	1.47×10^{-7}
54	20	3	1800	0.12	0.12	1000	40	1.5	1400	0.1	0.1		40	1	300	0.03	3.23×10^{-4}	1.47×10^{-7}
55	3	0.8	600	0.05	0.05	450	5	0.8	500	0.02	0.02		30	1	300	0.02	3.23×10^{-4}	1.47×10^{-7}
56	3	0.8	350	0.05	0.05	450	0.8	400	400	0.02			40	1	288	0.01	3.23×10^{-4}	1.47×10^{-7}

References

1. Jiang, W.; Pan, H.; Wang, Y.; Li, Y.; Lin, Y.; Bi, F. A Multi-Level Cross-Attention Image Registration Method for Visible and Infrared Small Unmanned Aerial Vehicle Targets via Image Style Transfer. *Remote Sens.* **2024**, *16*, 2880. [CrossRef]
2. Zhou, Y.; Wang, Q.; Li, T. A new model to simulate infrared radiation from an aircraft exhaust system. *Chin. J. Aeronaut.* **2017**, *30*, 651–662. [CrossRef]
3. Modest, M.F. The Treatment of Nongray Properties in Radiative Heat Transfer: From Past to Present. *J. Heat Transf.-Trans. ASME* **2013**, *135*, 061801. [CrossRef]
4. Hartmann, J.M.; Levi Di Leon, R.; Taine, J. Line-by-line and narrow-band statistical model calculations for H_2O. *J. Quant. Spectrosc. Radiat. Transf.* **1984**, *32*, 119–127. [CrossRef]
5. Soufiani, A.; Taine, J. High temperature gas radiative property parameters of statistical narrow-band model for H_2O, CO_2 and CO, and correlated-*k* model for H_2O and CO_2. *Int. J. Heat Mass Transf.* **1997**, *40*, 987–991. [CrossRef]
6. Modest, M.F. Narrow-band and full-spectrum *K*-distributions for radiative heat transfer–correlated-*k* vs. scaling approximation. *J. Quant. Spectrosc. Radiat. Transf.* **2003**, *76*, 69–83. [CrossRef]
7. Marin, O.; Buckius, R.O. Wide Band Correlated-k Approach to Thermal Radiative Transport in Nonhomogeneous Media. *J. Heat Transf.* **1997**, *119*, 719–729. [CrossRef]
8. André, F. The *L*-distribution method for modeling non-gray absorption in uniform and non-uniform gaseous media. *J. Quant. Spectrosc. Radiat. Transf.* **2016**, *179*, 19–32. [CrossRef]
9. Curtis, A. A statistical model for watervapour absorption. *Q. J. R. Met. Soc.* **1952**, *78*, 639–640.
10. Godson, W.L. The computation of infrared transmission by atmospheric water vapor. *J. Atmos. Sci.* **1955**, *12*, 272–284. [CrossRef]
11. Malkmus, W. Random Lorentz band model with exponential-tailed S-1 line-intensity distribution function. *JOSA* **1967**, *57*, 323–329. [CrossRef]
12. Penner, S.; Landshoff, R. Quantitative molecular spectroscopy and gas emissivities. *Phys. Today* **1960**, *13*, 38–40. [CrossRef]
13. Edwards, D.; Menard, W. Comparison of models for correlation of total band absorption. *Appl. Opt.* **1964**, *3*, 621–625. [CrossRef]
14. Edwards, D.; Balakrishnan, A. Thermal radiation by combustion gases. *Int. J. Heat Mass Transf.* **1973**, *16*, 25–40. [CrossRef]
15. Yin, X.M.; Liu, L.H.; Li, B.X. Numerical simulation of infrared signature emitted by liquid rocket plume using wide band K-distribution model. *Adv. Mater. Res.* **2012**, *516*, 41–53. [CrossRef]
16. Modest, M.F.; Mazumder, S. *Radiative Heat Transfer*; Academic Press: Cambridge, MA, USA, 2021.
17. Zhang, F.; Zhu, M.; Li, J.; Li, W.; Di, D.; Shi, Y.N.; Wu, K. Alternate Mapping Correlated k-Distribution Method for Infrared Radiative Transfer Forward Simulation. *Remote Sens.* **2019**, *11*, 994. [CrossRef]
18. Wang, Q.; Li, Y.; Hu, H. Numerical simulation of remote infrared imaging for marine exhaust system using wide-band k-distribution model combined with a new grouping method for spectral sub-intervals. *Infrared Phys. Technol.* **2019**, *96*, 276–290. [CrossRef]
19. Zhang, H.; Modest, M.F. A multi-scale full-spectrum correlated-*k* distribution for radiative heat transfer in inhomogeneous gas mixtures. *J. Quant. Spectrosc. Radiat. Transf.* **2002**, *73*, 349–360. [CrossRef]
20. Rivière, P.; Soufiani, A.; Taine, J. Correlated-k fictitious gas model for H_2O infrared radiation in the Voigt regime. *J. Quant. Spectrosc. Radiat. Transf.* **1995**, *53*, 335–346. [CrossRef]
21. Hu, H.; Wang, Q. Improved spectral absorption coefficient grouping strategy of wide band k-distribution model used for calculation of infrared remote sensing signal of hot exhaust systems. *J. Quant. Spectrosc. Radiat. Transf.* **2018**, *213*, 17–34. [CrossRef]
22. Zhang, H.; Modest, M.F. Scalable Multi-Group Full-Spectrum Correlated-k Distributions for Radiative Transfer Calculations. *J. Heat Transf.* **2003**, *125*, 454–461. [CrossRef]
23. Khodyko, Y.V.; Kurskov, A.A.; Antiporovich, N.V. Multigroup method for the calculation of selective IR radiation transfer in nonhomogeneous media. *J. Appl. Spectrosc.* **1986**, *44*, 284–288. [CrossRef]
24. Pierrot, L.; Rivière, P.; Soufiani, A.; Taine, J. A fictitious-gas-based absorption distribution function global model for radiative transfer in hot gases. *J. Quant. Spectrosc. Radiat. Transf.* **1999**, *62*, 609–624. [CrossRef]
25. Soufiani, A.; André, F.; Taine, J. A fictitious-gas based statistical narrow-band model for IR long-range sensing of H_2O at high temperature. *J. Quant. Spectrosc. Radiat. Transf.* **2002**, *73*, 339–347. [CrossRef]
26. West, R.; Crisp, D.; Chen, L. Mapping transformations for broadband atmospheric radiation calculations. *J. Quant. Spectrosc. Radiat. Transf.* **1990**, *43*, 191–199. [CrossRef]
27. André, F.; Hou, L.; Roger, M.; Vaillon, R. The multispectral gas radiation modeling: A new theoretical framework based on a multidimensional approach to *K*-Distrib. Methods. *J. Quant. Spectrosc. Radiat. Transf.* **2014**, *147*, 178–195. [CrossRef]
28. André, F.; Solovjov, V.P.; Webb, B.W.; Galtier, M.; Dubuisson, P. Spectral mapping method based on intervals of comonotonicity for modelling of radiative transfer in non-uniform gaseous media. *J. Quant. Spectrosc. Radiat. Transf.* **2019**, *229*, 33–39. [CrossRef]
29. Pierrot, L.; Soufiani, A.; Taine, J. Accuracy of narrow-band and global models for radiative transfer in H_2O, CO_2, and H_2O-CO_2 mixtures at high temperature. *J. Quant. Spectrosc. Radiat. Transf.* **1999**, *62*, 523–548. [CrossRef]
30. Shi, G.; Xu, N.; Wang, B.; Dai, T.; Zhao, J. An improved treatment of overlapping absorption bands based on the correlated *k* distribution model for thermal infrared radiative transfer calculations. *J. Quant. Spectrosc. Radiat. Transf.* **2009**, *110*, 435–451. [CrossRef]

31. Zhang, H.; Nakajima, T.; Shi, G.; Suzuki, T.; Imasu, R. An optimal approach to overlapping bands with correlated k distribution method and its application to radiative calculations. *J. Geophys. Res. Atmos.* **2003**, *108*. [CrossRef]
32. Pal, G.; Modest, M.F. A New Hybrid Full-Spectrum Correlated k-Distribution Method for Radiative Transfer Calculations in Nonhomogeneous Gas Mixtures. In Proceedings of the ASME/JSME 2007 Thermal Engineering Heat Transfer Summer Conference Collocated with the ASME 2007 InterPACK Conference, Vancouver, BC, Canada, 8–12 July 2007. [CrossRef]
33. Wang, L.; Modest, M.F. A Hybrid Multi-Scale Full-Spectrum k-Distribution Method for Radiative Transfer in Inhomogeneous Gas Mixtures. In Proceedings of the ASME International Mechanical Engineering Congress and Exposition, Orlando, FL, USA, 5–11 November 2005; Volume 42223, pp. 175–182.
34. Hu, H.; Li, Y.; Wei, Z.; Wang, Q. Parameter optimization for MSMGWB model used to calculate infrared remote sensing signals emitted by hot combustion gases of hydrocarbon fuel. *J. Quant. Spectrosc. Radiat. Transf.* **2020**, *249*, 107003. [CrossRef]
35. Wang, Q.; Hao, J.; Hu, H.; Li, Y.; Wu, Y.; Xie, Y.; Deng, H. Optimization of the MSMGWB models used to predict remote infrared signals of jet engine in various spectral intervals. *Infrared Phys. Technol.* **2024**, *140*, 105403. [CrossRef]
36. Deb, K.; Pratap, A.; Agarwal, S.; Meyarivan, T. A fast and elitist multiobjective genetic algorithm: NSGA-II. *IEEE Trans. Evol. Comput.* **2002**, *6*, 182–197. [CrossRef]
37. Washington, R.; Garmatyuk, D.; Mudaliar, S.; Narayanan, R.M. Many-Objective RadarCom Signal Design via NSGA-II Genetic Algorithm Implementation and Simulation Analysis. *Remote Sens.* **2022**, *14*, 3787. [CrossRef]
38. Rothman, L.S.; Gordon, I.E.; Barber, R.J.; Dothe, H.; Gamache, R.R.; Goldman, A.; Perevalov, V.I.; Tashkun, S.A.; Tennyson, J. HITEMP, the high-temperature molecular spectroscopic database. *J. Quant. Spectrosc. Radiat. Transf.* **2010**, *111*, 2139–2150. [CrossRef]
39. Volz, F.E. Infrared Refractive Index of Atmospheric Aerosol Substances. *Appl. Opt.* **1972**, *11*, 755–759. [CrossRef] [PubMed]
40. Wiscombe, W.J. Improved Mie scattering algorithms. *Appl. Opt.* **1980**, *19*, 1505–1509. [CrossRef] [PubMed]
41. Pal, G.; Modest, M.F. A Narrow Band-Based Multiscale Multigroup Full-Spectrum k-Distribution Method for Radiative Transfer in Nonhomogeneous Gas-Soot Mixtures. *J. Heat Transf.* **2009**, *132*, 023307. [CrossRef]
42. Hu, H.; Wang, Q. Improved spectral absorption-coefficient grouping strategies in radiation heat transfer calculations for combustion gases with pressure and temperature inhomogeneity. *Numer. Heat Transf. Part B Fundam.* **2019**, *75*, 178–197. [CrossRef]